

SILVERRUSH. III. Deep Optical and Near-Infrared Spectroscopy for Ly α and UV-Nebular Lines of Bright Ly α Emitters at $z = 6 - 7$

Takatoshi Shibuya¹, Masami Ouchi^{1,2}, Yuichi Harikane^{1,3}, Michael Rauch⁴, Yoshiaki Ono¹, Shiro Mukae^{1,5}, Ryo Higuchi^{1,3}, Takashi Kojima^{1,3}, Suraphong Yuma⁶, Chien-Hsiu Lee⁷, Hisanori Furusawa⁸, Akira Konno^{1,5}, Crystal L. Martin⁹, Kazuhiro Shimasaku^{5,10}, Yoshiaki Taniguchi¹¹, Masakazu A. R. Kobayashi¹², Masaru Kajisawa¹³, Tohru Nagao¹³, Tomotsugu Goto¹⁴, Nobunari Kashikawa^{8,15}, Yutaka Komiyama^{8,15}, Haruka Kusakabe⁵, Rieko Momose¹⁴, Kimihiko Nakajima¹⁶, Masayuki Tanaka^{8,15}, and Shiang-Yu Wang¹⁷

¹Institute for Cosmic Ray Research, The University of Tokyo, 5-1-5 Kashiwanoha, Kashiwa, Chiba 277-8582, Japan

²Kavli Institute for the Physics and Mathematics of the Universe (Kavli IPMU, WPI), University of Tokyo, Kashiwa, Chiba 277-8583, Japan

³Department of Physics, Graduate School of Science, The University of Tokyo, 7-3-1 Hongo, Bunkyo, Tokyo 113-0033, Japan

⁴Observatories of the Carnegie Institution of Washington, 813 Santa Barbara Street, Pasadena, CA 91101, USA

⁵Department of Astronomy, Graduate School of Science, The University of Tokyo, 7-3-1 Hongo, Bunkyo, Tokyo 113-0033, Japan

⁶Department of Physics, Faculty of Science, Mahidol University, Bangkok 10400, Thailand

⁷Subaru Telescope, NAOJ, 650 N Aohoku Pl., Hilo, HI 96720, USA

⁸National Astronomical Observatory, Mitaka, Tokyo 181-8588, Japan

⁹Department of Physics, University of California, Santa Barbara, CA, 93106, USA

¹⁰Research Center for the Early Universe, Graduate School of Science, The University of Tokyo, 7-3-1 Hongo, Bunkyo, Tokyo 113-0033, Japan

¹¹The Open University of Japan, Wakaba 2-11, Mihama-ku, Chiba 261-8586, Japan

¹²Faculty of Natural Sciences, National Institute of Technology, Kure College, 2-2-11 Agaminami, Kure, Hiroshima 737-8506, Japan

¹³Research Center for Space and Cosmic Evolution, Ehime University, Bunkyo-cho 2-5, Matsuyama 790-8577, Japan

¹⁴Institute of Astronomy, National Tsing Hua University, 101 Section 2, Kuang-Fu Road, Hsinchu 30013, Taiwan

¹⁵The Graduate University for Advanced Studies (SOKENDAI), 2-21-1 Osawa, Mitaka, Tokyo 181-8588

¹⁶European Southern Observatory, Karl-Schwarzschild-Str. 2, D-85748, Garching bei Munchen, Germany

¹⁷Academia Sinica, Institute of Astronomy and Astrophysics, 11F of AS/NTU Astronomy-Mathematics Building, No.1, Sec. 4, Roosevelt Rd, Taipei 10617, Taiwan

†Based on data obtained with the Subaru Telescope. The Subaru Telescope is operated by the National Astronomical Observatory of Japan.

‡This paper includes data gathered with the 6.5 meter Magellan Telescopes located at Las Campanas Observatory, Chile.

*E-mail: shibyatk@icrr.u-tokyo.ac.jp

Received (reception date); Accepted (acceptation date)

Abstract

We present Ly α and UV-nebular emission line properties of bright Ly α emitters (LAEs) at $z = 6 - 7$ with a luminosity of $\log L_{\text{Ly}\alpha}/[\text{erg s}^{-1}] = 43 - 44$ identified in the 21-deg² area of the SILVERRUSH early sample developed with the Subaru Hyper Suprime-Cam (HSC) survey data. Our optical spectroscopy newly confirm 21 bright LAEs with clear Ly α emission, and contribute to make a spectroscopic sample of 96 LAEs at $z = 6 - 7$ in SILVERRUSH. From the spectroscopic sample, we select 7 remarkable LAEs as bright as Himiko and CR7 objects, and perform deep Keck/MOSFIRE and Subaru/nuMOIRCS near-infrared spectroscopy reaching the 3σ -flux limit of $\sim 2 \times 10^{-18}$ erg s⁻¹ for the UV-nebular emission lines of He II λ 1640, C IV λ 1548, 1550, and O III] λ 1661, 1666. Except for one tentative detection of C IV, we find no strong UV-nebular lines down to the flux limit, placing the upper limits of the rest-frame equivalent widths (EW_0) of $\sim 2 - 4$ Å for C IV, He II, and O III] lines. Here we also investigate the VLT/X-SHOOTER spectrum of CR7 whose 6σ detection of He II is claimed by Sobral et al. Although two individuals and the ESO-archive service carefully re-analyze the X-SHOOTER data that are used in the study of Sobral et al., no He II signal of CR7 is detected, supportive of weak UV-nebular lines of the bright LAEs even for CR7. Spectral properties of these bright LAEs are thus clearly different from those of faint dropouts at $z \sim 7$ that have strong UV-nebular lines shown in the various studies. Comparing these bright LAEs and the faint dropouts, we find anti-correlations between the UV-nebular line EW_0 and UV-continuum luminosity, which are similar to those found at $z \sim 2 - 3$.

Key words: early universe — galaxies: formation — galaxies: high-redshift

1 Introduction

Bright Ly α -emitting galaxies are important objects in the studies of the early Universe and galaxy formation. The bright Ly α emission with $\log L_{\text{Ly}\alpha}/[\text{erg s}^{-1}] \simeq 43 - 44$ is expected to be reproduced in various physical mechanisms (e.g., Fisher et al. 2014; Pallottini et al. 2015b). Very young and metal-free stars (Population III; Pop III) hosted in galaxies would emit the substantially strong Ly α radiation with a narrow He II λ 1640 line ($\lesssim 200$ km s⁻¹) and a Ly α equivalent width (EW) enhancement. On the other hand, active galactic nuclei (AGNs) would also produce the bright Ly α emission with high ionization metal lines such as N V λ 1238, 1240 and C IV λ 1548, 1550 due to the strong UV radiation from the central ionizing source. In addition, the highly-complex Ly α radiative transfer in the interstellar medium (ISM) makes it difficult to understand the Ly α emitting mechanism (e.g., Neufeld 1991; Hansen & Oh 2006).

Ly α emitters (LAEs) have been surveyed by imaging observations with dedicated narrow-band (NB) filters. During the last decades, a wide FoV of Subaru/Suprime-Cam (SCam) has al-

lowed us to identify LAE candidates at the bright-end of Ly α luminosity functions (LFs; e.g., Taniguchi et al. 2005; Shimasaku et al. 2006; Murayama et al. 2007; Ota et al. 2008; Ouchi et al. 2008; Ouchi et al. 2010; Hu et al. 2010; Kashikawa et al. 2006; Kashikawa et al. 2011; Konno et al. 2014; Matthee et al. 2015). Follow-up optical spectroscopic observations have confirmed several bright LAEs at $z \simeq 6.6$ (e.g., *Himiko*: Ouchi et al. 2009; *CR7* and *MASOSA*: Sobral et al. 2015; *COLAI*: Hu et al. 2016; Bagley et al. 2017), and at $z \simeq 5.7$ (Mallery et al. 2012).

However, subsequent multi-band observations find the heterogeneity in the nature of these bright LAEs. Zabl et al. (2015) have reported no detections of He II nor C IV from *Himiko* with VLT/X-SHOOTER. A deep ALMA observation reveals that *Himiko* has no strong [C II] λ 158 μ m line and dust continuum emission (Ouchi et al. 2013). Combined with morphological properties, the bright Ly α emission of *Himiko* is probably caused by intense star formation in a galaxy merger. On the other hand, Sobral et al. (2015) have claimed that a narrow He II line is detected at the 6σ significance level from CR7 based

on a deep VLT/X-SHOOTER near-infrared (NIR) spectroscopy. The He II detection might suggest that CR7 host Pop III stellar populations. Recently, a number of theoretical studies interpret the strong He II emission from CR7 (e.g., Pallottini et al. 2015a; Agarwal et al. 2016; Hartwig et al. 2016; Johnson & Dijkstra 2016; Dijkstra et al. 2016; Smidt et al. 2016; Smith et al. 2016; Visbal et al. 2016; Pacucci et al. 2017; Visbal et al. 2017). In contrast to the claim of the He II detection, CR7 clearly includes old stellar population found from analyses for photometric data (Bowler et al. 2016), suggesting that this system would not be truly young. These studies indicate that the nature of bright LAEs has become a hot topic of debate.

Even in the substantial observational and theoretical efforts, the diversity of the bright LAEs has not been unveiled yet due to the small statistics. In this paper, we present the results of our optical and NIR spectroscopic observations for bright LAEs selected with data of a new wide-FoV camera, Hyper Suprime-Cam (HSC), on the Subaru Telescope. In our spectroscopic observations, we newly identify 21 bright LAEs with $\log L_{\text{Ly}\alpha}/[\text{erg s}^{-1}] \simeq 43 - 44$, which have enlarged the spectroscopic sample of bright LAEs by a factor of four.

This is the third paper in our ongoing HSC research project for Ly α -emitting objects, *Systematic Identification of LAEs for Visible Exploration and Reionization Research Using Subaru HSC (SILVERRUSH)*. In this project, we study various properties of high- z LAEs, e.g., LAE clustering (Ouchi et al. 2017), photometric properties of Ly α line EW and Ly α spatial extent (Shibuya et al. 2017), spectroscopic properties of bright LAEs (this study), Ly α LFs (Konno et al. 2017), and LAE overdensity (R. Higuchi et al. in preparation). This program is one of the twin programs. Another program is the study for dropouts, Great Optically Luminous Dropout Research Using Subaru HSC (GOLDRUSH), that is detailed in Ono et al. (2017) and Harikane et al. (2017). Source catalogs for the LAEs and dropouts will be presented on our project webpage at <http://cos.icrr.u-tokyo.ac.jp/rush.html>.

This paper has the following structure. In Section 2, we describe the HSC data and target selections of bright LAEs for our optical and NIR spectroscopy. Section 3 presents details of the spectroscopic observations for the bright LAEs and the data reduction. In Section 4, we investigate physical properties for bright LAEs at $z \simeq 6$ using our statistical sample of bright LAEs. In Section 5, we discuss the implications for galaxy formation and evolution. We summarize our findings in Section 6.

Throughout this paper, we adopt the concordance cosmology with $(\Omega_{\text{m}}, \Omega_{\Lambda}, h) = (0.3, 0.7, 0.7)$ (Planck Collaboration et al. 2016). All magnitudes are given in the AB system (Oke & Gunn 1983).

2 Targets for Spectroscopy

2.1 Imaging Data

In March 2014, the Subaru telescope has started a large-area NB survey with HSC in a Subaru strategic program (SSP; Aihara et al. 2017b). This survey will construct a sample of LAEs at $z \simeq 2.2, 5.7, 6.6$, and 7.3 with four NB filters of *NB387*, *NB816*, *NB921*, and *NB101*. The statistical LAE sample allows us to study the LAE evolution and physical processes of the cosmic reionization.

In this study, we use the HSC SSP S16A broadband (BB; Kawanomoto 2017) and *NB921* and *NB816* data that are obtained in 2014–2016. Note that this HSC SSP S16A data is significantly larger than the first-released data in Aihara et al. (2017a).

The HSC images were reduced with the HSC pipeline, *hscPipe* 4.0.2 (Bosch et al. 2017) which is a code from the Large Synoptic Survey Telescope (LSST) software pipeline (Ivezic et al. 2008; Axelrod et al. 2010; Jurić et al. 2015). The photometric calibration is carried out with the PanSTARRS1 processing version 2 imaging survey data (Magnier et al. 2013; Schlafly et al. 2012; Tonry et al. 2012). The details of the data reduction are provided in Aihara et al. (2017a); Bosch et al. (2017); Aihara et al. (2017a).

The *NB921* (*NB816*) filter has a central wavelength of $\lambda_c = 9215\text{\AA}$ (8177\AA) and an FWHM of 135\AA (113\AA), which traces the redshifted Ly α emission line at $z = 6.580 \pm 0.056$ ($z = 5.726 \pm 0.046$). The transmission curves and the detailed specifications of these NB filters are presented in Ouchi et al. (2017). The method of the transmission curve measurements is given by Kawanomoto (2017).

The HSC SSP S16A *NB921* and *NB816* data cover a total survey area of $\simeq 21.2$ and $\simeq 13.8$ deg², respectively. The survey area consists of two Ultradeep (UD) fields: UD-COSMOS, and UD-SXDS, and three Deep (D) fields: D-ELAIS-N1, D-DEEP2-3, and D-COSMOS. The FWHM of the typical seeing size is $\simeq 0''.6$. The 5σ NB limiting magnitudes for the UD and D fields are typically $\simeq 25.5$ and $\simeq 25.0$ mag in a $1''.5$ -diameter aperture, respectively. The details of the HSC NB data are presented in Shibuya et al. (2017). This HSC *NB921* and *NB816* data provide the largest NB survey area for $z \simeq 5.7 - 6.6$ LAEs even before the completion of the SSP observation.

2.2 Selection of Bright LAEs

Using the HSC NB data, we select targets of bright LAE candidates with $\log L_{\text{Ly}\alpha}/[\text{erg s}^{-1}] \simeq 43 - 44$ for follow-up spectroscopic observations. The details of the LAE selection are given in Shibuya et al. (2017), but we provide a brief description as follows. To identify objects with an NB magnitude excess in the HSC catalog, we apply the magnitude and color selection criteria similar to those of Ouchi et al. (2008) and Ouchi et al.

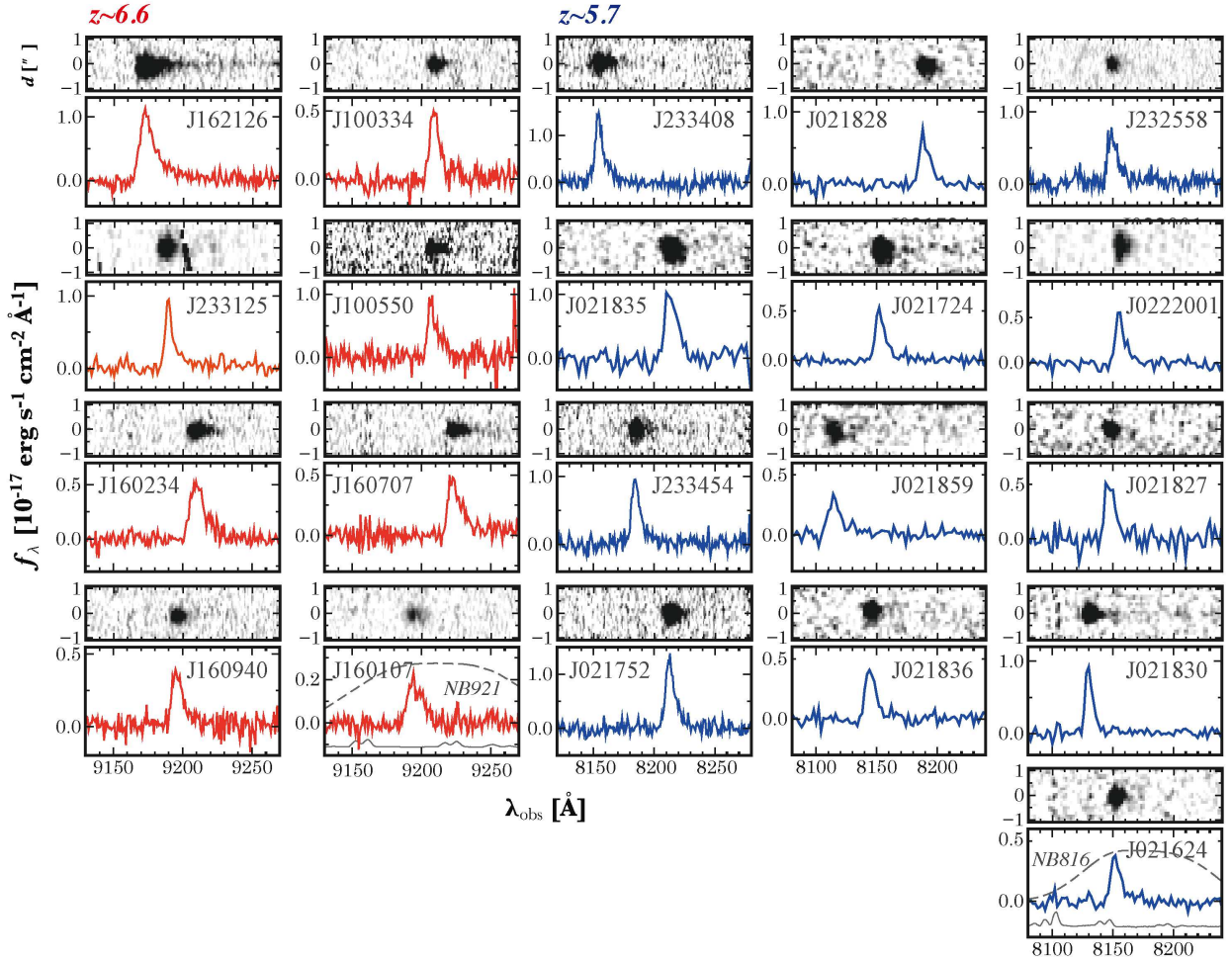


Fig. 1. Ly α spectra for the 21 newly-identified bright LAEs with $\log L_{\text{Ly}\alpha}/[\text{erg s}^{-1}] \simeq 43 - 44$. The red and blue lines represent the Ly α spectra of the bright LAEs at $z \simeq 6.6$ and $z \simeq 5.7$, respectively. The dashed gray curves indicate the transmission curves of *NB921* and *NB816*. The solid gray lines denote the sky OH emission lines. The x-axis indicates the wavelength observed in air. The heliocentric motion of the Earth is not corrected in this figure.

(2010). To remove spurious sources such as satellite trails and cosmic rays, we perform visual inspections to multi-band HSC images of *grizy* and *NB* for the objects selected in the magnitude and color selection criteria. We have also checked multi-epoch images to remove transients and asteroid-like moving objects. In total, photometric candidates of 1,153 and 1,077 LAEs at $z \simeq 6.6$ and $z \simeq 5.7$ are identified in the HSC-*NB921* and *NB816* fields, respectively. Finally, we select bright LAE candidates with an NB magnitude of $NB \leq 24$ mag corresponding to $\log L_{\text{Ly}\alpha}/[\text{erg s}^{-1}] \simeq 43 - 44$.

3 Spectroscopic Data

We carried out optical and NIR spectroscopic observations for the bright LAE candidates at $z \simeq 5.7 - 6.6$ selected with the HSC NB data. These optical and NIR observations mainly 1) make spectroscopic confirmations through Ly α and 2) investigate properties of ionizing sources (e.g., the presence of metal-

poor galaxies and AGN activity), respectively, for bright LAEs. Table 1 summarizes the instruments, the exposure time and line flux limits of our spectroscopic observations for each target.

In the following sections of Sections 3.1 and 3.2, we describe the details of optical and NIR spectroscopic data, respectively.

3.1 Optical Spectroscopic Data

We performed optical follow-up spectroscopy for bright LAE candidates at $z \simeq 5.7 - 6.6$ to detect Ly α emission lines. The choice of the targets depends on the target visibility during the allocated time for individual spectroscopic observations. Basically, we selected the brightest LAE candidates as the targets in each observing run.

3.1.1 Subaru/FOCAS

We used the Faint Object Camera and Spectrograph (FOCAS; Kashikawa et al. 2002) on the Subaru telescope to observe

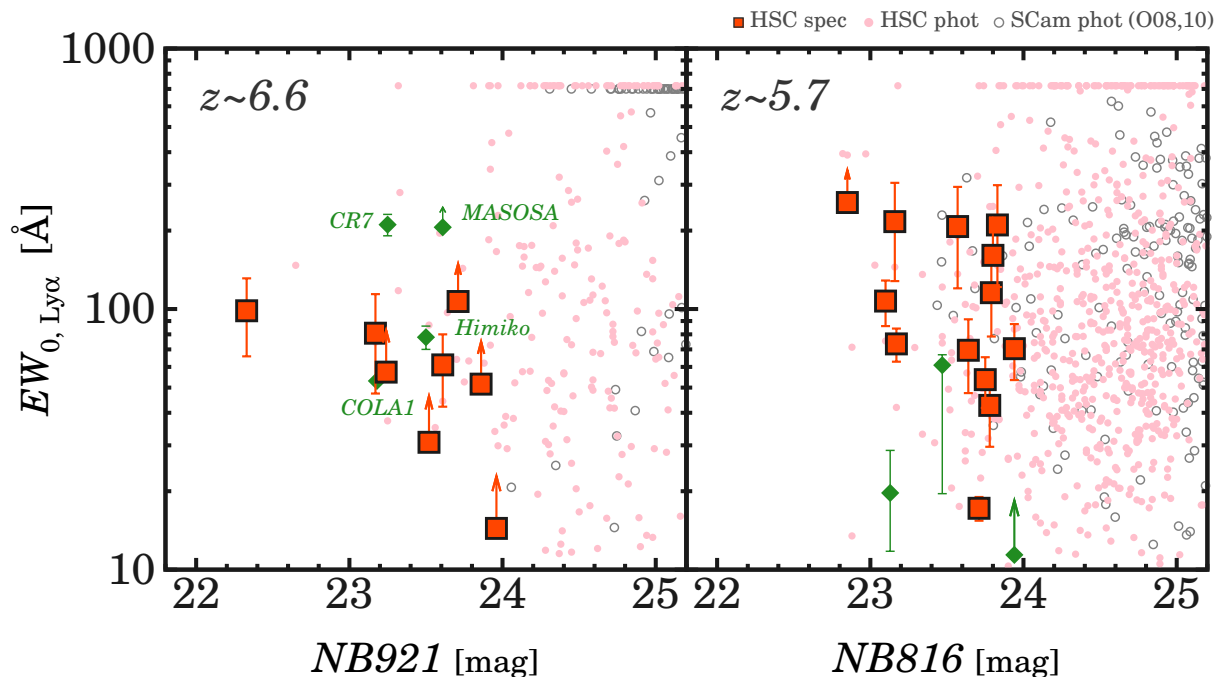


Fig. 2. NB magnitude and $\text{Ly}\alpha$ EW for LAEs at $z \simeq 6.6$ (left) and $\simeq 5.7$ (right). The red squares represent the 21 newly identified bright LAEs. The green diamonds indicate $NB < 24$ bright LAEs which have been spectroscopically confirmed by previous studies (Ouchi et al. 2009; Mallery et al. 2012; Sobral et al. 2015; Hu et al. 2016). The magenta filled circles present LAE candidates in HSC LAE catalogs constructed by Shibuya et al. (2017). The gray open circles denote LAE candidates found in SCam NB surveys (Ouchi et al. 2008; Ouchi et al. 2010). The objects with $EW_{0, \text{Ly}\alpha} > 700 \text{ \AA}$ are plotted at $EW_{0, \text{Ly}\alpha} = 700 \text{ \AA}$.

16 LAE candidates. Out of the 16 objects, we observed 15 LAEs on 2016 June 21–22 and September 8 (S16A-060N and S16B-029N, PI: T. Shibuya), and one as a filler target of a FOCAS observation in 2015 December (S15B-059 in PI: S. Yuma; see Yuma et al. 2017). These observations were made with the VPH900 grism with the O58 order-cut filter, giving spectral coverage of 7500–10450 Å with a dispersion of 0.74 Å pix^{-1} . The 0''8-wide slit used gave a spectroscopic resolution of $R \simeq 1800$ which is sufficient to distinguish [O II] doublet lines from low- z galaxy contaminants at $z \simeq 0.6 - 0.8$. The observing nights were photometric, with good seeing of $\sim 0.''6 - 1.''0$. The Multi-Object Spectroscopy (MOS) mode was used to align securely the slits on our high- z sources. Each of the 20 minute exposures was taken by dithering the telescope pointing along the slit by $\pm 1.''0$. The standard star Feige34 was taken at the beginning and end of each observed night (Massey & Gronwall 1990).

Our FOCAS spectra were reduced in a standard manner with the IRAF¹ package (e.g., Kashikawa et al. 2006; Shibuya et al. 2012). First, we performed flat-fielding with flat images, corrected for the image distortion, calibrated wavelengths with sky OH lines, and rejected sources illuminated by the cosmic ray injections. Next, we subtracted the sky background. After the sky background subtraction, we stacked the two-dimensional (2D) spectra. From each 2D data, we then extracted one-dimensional

(1D) spectra using an extraction width of $\simeq \pm 0.''4 - \pm 0.''8$ in the spatial direction of the slits. The extraction width is determined based on the extent of targets and the seeing conditions during the observations. Similarly, these extraction widths are used for the data obtained from the other optical and NIR spectrographs (Sections 3.1 and 3.2). Finally, we carried out flux calibrations for the 1D spectra using the data of standard stars.

The slit loss of the emission line flux has automatically been corrected in the flux calibration. This is because we observe the standard stars in the observing configuration (i.e. slit-width) and sky condition that are the same as those for our main targets. Note that our high- z main targets are point source-like objects whose slit loss is the same as that of the standard stars. For this reason, we do not perform data reduction procedures for the slit loss correction for our optical and NIR spectra in Sections 3.1 and 3.2.

3.1.2 Magellan/LDSS3

We also used the Low Dispersion Survey Spectrograph 3 (LDSS3) on the Magellan II (Clay) telescope in October 2016 (PI: M. Rauch) to take spectroscopy for two bright LAE candidates. The seeing was $\sim 0.''6 - 1.''0$. We set the instrumental configuration to observe wavelength ranges of 8000–10000 Å. The spatial pixel scale was 0.''189 pix^{-1} , and the spectral dispersion was 0.47 Å pix^{-1} . The slit width is 0.''8.

¹ <http://iraf.noao.edu>

3.1.3 Magellan/IMACS

In addition to the Subaru/FOCAS and Magellan/LDSS3 observations, we use spectroscopic data obtained with the Inamori Magellan Areal Camera & Spectrograph (IMACS; Dressler et al. 2011) on the Magellan I Baade Telescope. The observations were conducted for high- z galaxies in the SXDS field in 2007 - 2011 (PI: M. Ouchi; R. Higuchi et al in preparation). In the HSC LAE and IMACS catalog matching, we obtained optical spectra for eight bright LAEs.

3.1.4 LAE Spectroscopic Confirmations

In total, we newly confirm 21 bright LAEs with a clear Ly α emission line in our Subaru/FOCAS and Magellan/LDSS3 observations and our Magellan/IMACS data. The 1D and 2D optical spectra of the 21 bright LAEs are shown in Figure 1. A prominent asymmetric emission line is found at $\simeq 9210\text{\AA}$ and $\simeq 8160\text{\AA}$ for each LAE at $z \simeq 6.6$ and $z \simeq 5.7$, respectively. These emission lines are detected at the $\simeq 10 - 20\sigma$ significance levels. No other emission line feature is found in the range of observed wavelengths. We obtain the redshift of the bright LAEs by fitting the symmetric Gaussian profile to the observed Ly α emission lines in the wavelength ranges where the flux drops to 70% of its peak value (Shibuya et al. 2014b). Figure 2 shows the NB magnitude and Ly α EW which is obtained in Section 4.1. As shown in Figure 2, our newly confirmed bright LAEs are as bright as e.g., Himiko and CR7.

We also check whether our LAEs selected with the HSC data, HSC LAEs, are spectroscopically confirmed in previous studies for the COSMOS and SXDS fields (Murayama et al. 2007; Taniguchi et al. 2009; Ouchi et al. 2008; Ouchi et al. 2010; Mallery et al. 2012; Sobral et al. 2015; Hu et al. 2016). In spectroscopic samples obtained by the previous studies, we find that 7 bright LAEs with $NB < 24$ mag and 69 faint ones with $NB > 24$ mag. In total, 96 LAEs are confirmed in our spectroscopic observations and the previous studies. Table 2 summarizes the number of the spectroscopically confirmed HSC LAEs.

The photometric properties and the HSC images for the bright LAEs in Table 4 and Figure 3, respectively. Although most of the bright LAEs are not detected in blue bands of g and r , COLA1 is marginally detected in the r -band image at $\simeq 2.5\sigma$.

Combining our 21 newly identified and the 7 previously confirmed bright LAEs (i.e., Himiko, CR7, MASOSA, COLA1, and three $z \simeq 5.7$ Mallery et al.'s objects), we construct a sample of 28 bright LAEs. The HSC data and our observations have enlarged a spectroscopic sample of bright LAEs by a factor of four. The large sample allows for a statistical study on physical properties of bright LAEs with $\log L_{\text{Ly}\alpha}/[\text{erg s}^{-1}] \simeq 43 - 44$.

3.1.5 Contamination Rates in the LAE Candidates

We estimate contamination rates, f_{contami} , in the HSC LAE candidates using the spectroscopic data. In our Subaru/FOCAS

and Magellan/LDSS3 observations for 12 $z \simeq 6.6$ and 6 $z \simeq 5.7$ bright LAE candidates with $NB < 24$ mag, we identify 4 and 1 low- z contaminants, respectively. Figure 4 presents the spectra and HSC cutout images for the low- z contaminants. All of the 5 contaminants are strong [O III] $\lambda\lambda 4959, 5007$ emitters at $z \simeq 0.6 - 0.8$ with faint BB magnitudes. The H β and H γ emission lines are not significantly detected in the short integration time (i.e. $\simeq 20 - 40$ minutes) of the FOCAS and LDSS3 observations. The photometric properties of these low- z contaminants are listed in Table 5. We find that $f_{\text{contami}} \simeq 33\%$ ($= 4/12$) and $\simeq 17\%$ ($= 1/6$) for bright LAE candidates with $NB < 24$ mag at $z \simeq 6.6$ and $z \simeq 5.7$, respectively.

We also calculate f_{contami} in the HSC LAE candidates including our Magellan/IMACS spectroscopic data (Section 3.1.3). This spectroscopic sample includes faint HSC LAE candidates with $NB > 24$ mag. Combining our Subaru/FOCAS and Magellan/LDSS3 data and the cross-matching of the Magellan/IMACS spectroscopic catalogs, we find that 28 and 53 HSC LAE candidates at $z \simeq 6.6$ and $z \simeq 5.7$ are spectroscopically observed. In total, we find that 4 out of 28 (4 out of 53) HSC LAE candidates are low- z contaminants, and estimate f_{contami} to be $\simeq 14\%$ and $\simeq 8\%$ for the samples of $z \simeq 6.6$ and $z \simeq 5.7$ LAEs, respectively.

In these estimates with the spectroscopic data, we find that $f_{\text{contami}} \simeq 0 - 30\%$. Table 3 summarizes the contamination rates. These f_{contami} values are used for the contamination correction for e.g., LAE clustering (Ouchi et al. 2017), Ly α LFs (Konno et al. 2017), and LAE overdensity (R. Higuchi et al. in prep.).

3.2 NIR Spectroscopic Data

We performed deep NIR spectroscopy to investigate whether the rest-frame UV-nebular emission lines (i.e., C IV $\lambda\lambda 1548, 1550$, He II $\lambda 1640$, and O III] $\lambda\lambda 1661, 1666$) exist in bright LAEs. As a first attempt, we observed seven out of the spectroscopically confirmed 21 bright LAEs. The LAEs observed by NIR spectrographs are listed in Table 1. The choice of the targets depends on the target visibility during the allocated time for individual spectroscopic observations. Basically, we have selected the brightest LAEs as the targets in each observing run.

3.2.1 Keck/MOSFIRE

We used the Multi-Object Spectrometer For Infra-red Exploration (MOSFIRE; McLean et al. 2012) on the Keck I telescope to observe 4 LAEs on 2016 September 9 (S16B-029N, PI: T. Shibuya) and an LAE on 2015 January 3-4 as a filler target (S15B-075, PI: M. Ouchi). Similar to the Subaru/FOCAS observations, the MOS mode was utilized to align securely the slits on our high- z sources. We used the Y

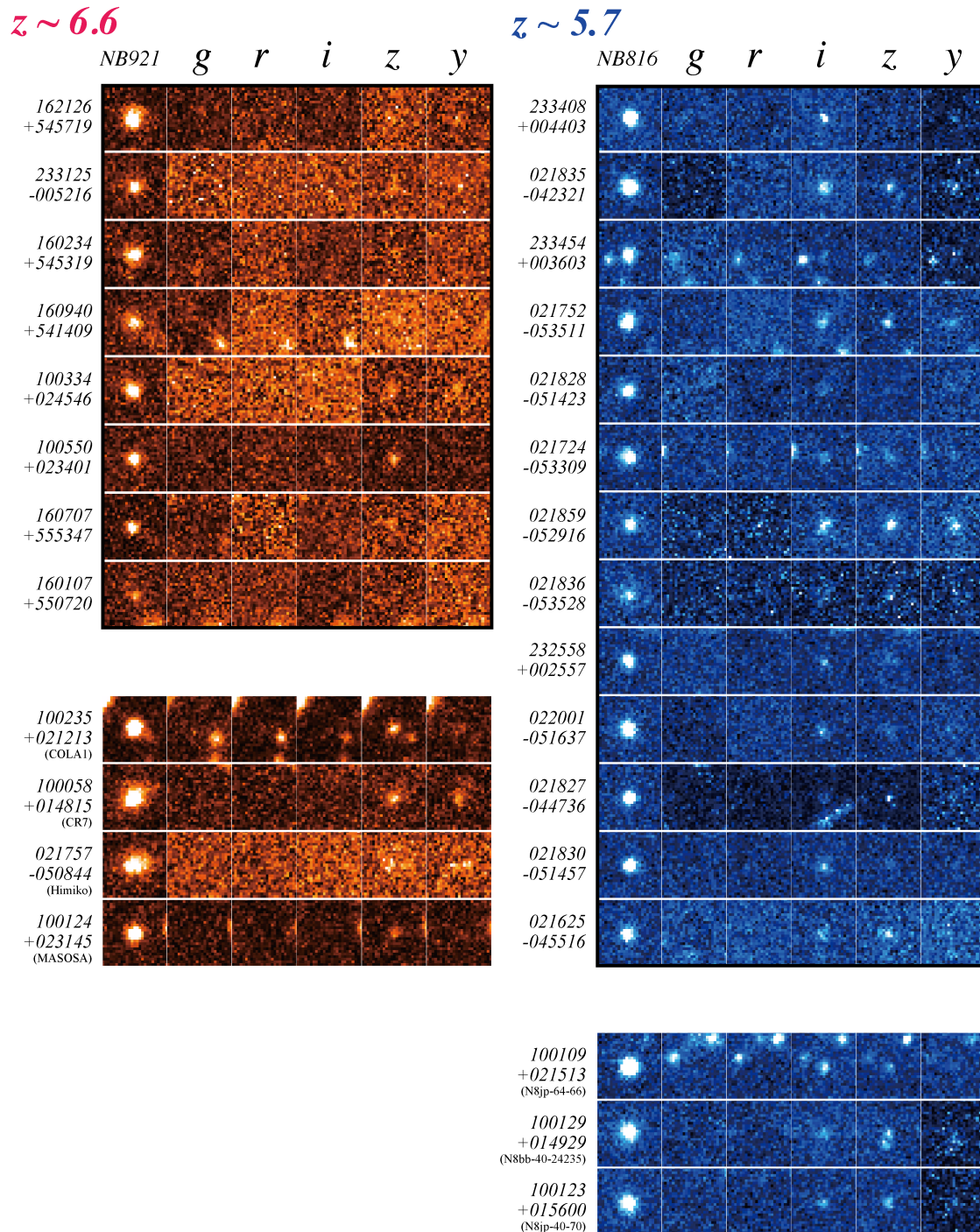


Fig. 3. HSC cutout images of the spectroscopically confirmed bright LAEs with $NB < 24$ mag at $z \simeq 6.6$ (left) and $z \simeq 5.7$ (right). Seven objects at the bottom are the previously identified bright LAEs at $z \simeq 6.6$ (Hu et al. 2016; Sobral et al. 2015; Ouchi et al. 2009) and at $z \simeq 5.7$ (Mallery et al. 2012). The image size is $4'' \times 4''$. The scale of flux density is arbitrary.

and J band filters for LAEs at $z \simeq 5.7$ and $z \simeq 6.6$, respectively. The seeing size was $\sim 0''.5$ - $0''.6$. The $0''.8$ -wide slit was used, giving a spectral resolution of $R \simeq 3500$.

The data of objects and standard stars were reduced using

the MOSFIRE data reduction pipeline.² We conducted standard reduction processes for the MOSFIRE spectra with sets of default pipeline parameters (see e.g., Kojima et al. 2016). Using A -spectral type stars which were taken in this observing run, we

² <https://keck-datareductionpipelines.github.io/MosfireDRP>

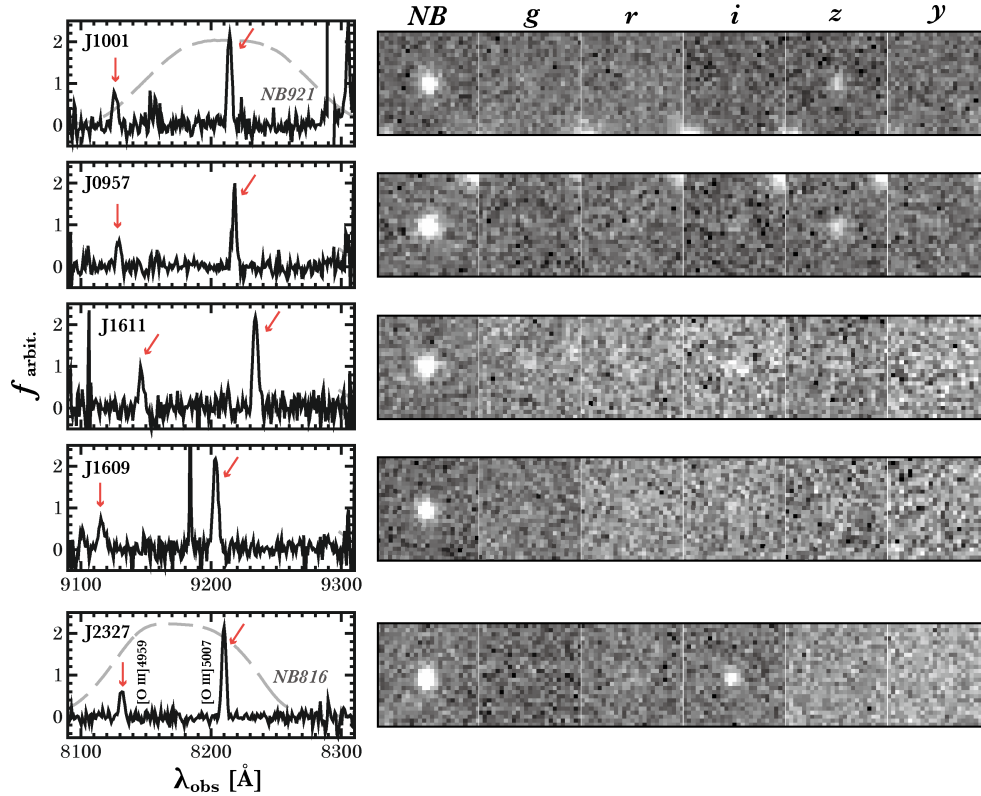


Fig. 4. (Left) Spectra for the 5 low- z contaminants in the Subaru/FOCAS and Magellan/LDSS3 observations. The red arrows indicate the positions of [O III] $\lambda\lambda$ 4959, 5007 emission lines. The dashed gray curves denote the transmission curves of NB921 and NB816. The x-axis indicates the wavelength observed in air. The heliocentric motion of the Earth is not corrected in this figure. The y-axis represents the flux density in arbitrary units. (Right) HSC cutout images of the low- z contaminants. The image size is $4'' \times 4''$. The scale of flux density is arbitrary. The photometric properties of the low- z contaminants are summarized in Table 5.

performed flux calibrations for the spectra of the target LAEs.

3.2.2 Subaru/nuMOIRCS

We used the upgraded version of the Multi-Object InfraRed Camera and Spectrograph (nuMOIRCS; Ichikawa et al. 2006; Suzuki et al. 2008; Fabricius et al. 2016; Walawender et al. 2016) on the Subaru telescope on 2016 June 21–22 to observe 2 LAEs at $z \simeq 6.6$ (S16A-060N, PI: T. Shibuya). The MOS mode was used to align securely the slits on our high- z sources. There were thin sky cirrus, but the weather condition was photometric. The seeing size was $\sim 0''.5$ – $1''.0$. The width of each slit in the MOS masks is $0''.8$. We used the VPH-J grism, giving the spectral resolution of $R \simeq 3000$. The standard star HIP115119 was observed on each night for flux calibrations.

We reduced the nuMOIRCS spectra with IRAF in the manner similar to the FOCAS data reduction (Section 3.1.1). We performed bias subtraction, flat fielding, image distortion correction, cosmic ray rejection, wavelength calibration, sky subtraction, and flux calibration.

4 Results

4.1 Physical Properties

We present physical quantities related to the Ly α emission: Ly α flux, $f_{\text{Ly}\alpha}$, Ly α luminosity, $L_{\text{Ly}\alpha}$, and the rest-frame Ly α EW, $EW_{0,\text{Ly}\alpha}$, for the bright LAEs with a spectroscopic redshift. To obtain these quantities, we scale the observed Ly α spectra to match the NB and BB magnitudes. Here we assume the rest-frame UV spectral slope of $\beta = -2$. The β parameter is defined by $f_{\lambda} \propto \lambda^{\beta}$ where f_{λ} is a galaxy spectrum at $\simeq 1500 - 3000\text{\AA}$. The 2σ lower limits of y (z)-band magnitudes are used for $z \simeq 6.6$ ($z \simeq 5.7$) LAEs whose UV continuum emission is not detected. For HSC J162126+545719 whose UV continuum is detected in the spectroscopic data (see Figure 1), we use the UV continuum flux density in the spectra to measure the $EW_{0,\text{Ly}\alpha}$ and M_{UV} values. Table 6 presents the quantities of $f_{\text{Ly}\alpha}$, $L_{\text{Ly}\alpha}$, and $EW_{0,\text{Ly}\alpha}$ for our 21 bright LAEs including a sample of 7 LAEs identified by previous studies (Ouchi et al. 2009; Mallery et al. 2012; Sobral et al. 2015; Hu et al. 2016). Figure 2 shows $EW_{0,\text{Ly}\alpha}$ as a function of NB magnitude. The $EW_{0,\text{Ly}\alpha}$ value ranges from $\simeq 10\text{\AA}$ to $\simeq 300\text{\AA}$.

Table 6 also shows whether the bright LAEs are spatially

Table 1. Our Optical and NIR Spectroscopic Observations for Bright LAEs

Object ID	Opt. Inst.	$T_{\text{exp,opt}}$ (minutes)	$f_{\text{lim,opt}}$ ($\text{erg s}^{-1} \text{cm}^{-2}$)	NIR. Inst.	$T_{\text{exp,NIR}}$ (minutes)	$f_{\text{lim,NIR}}$ ($\text{erg s}^{-1} \text{cm}^{-2}$)
(1)	(2)	(3)	(4)	(5)	(6)	(7)
HSC J162126+545719	FOCAS	60	$\simeq 1.2 \times 10^{-18}$	MOSFIRE	120	$\simeq 1.8 \times 10^{-18}$
HSC J233125-005216	LDSS3	90	$\simeq 0.5 \times 10^{-18}$	—	—	—
HSC J160234+545319	FOCAS	60	$\simeq 0.3 \times 10^{-18}$	nuMOIRCS	180	$\simeq 5.3 \times 10^{-18}$
HSC J160940+541409	FOCAS	60	$\simeq 0.6 \times 10^{-18}$	nuMOIRCS	300	$\simeq 6.0 \times 10^{-18}$
HSC J100334+024546	FOCAS	100	$\simeq 1.3 \times 10^{-18}$	—	—	—
HSC J100550+023401	FOCAS	60	$\simeq 1.0 \times 10^{-18}$	MOSFIRE	120	$\simeq 0.3 \times 10^{-18}$
HSC J160707+555347	FOCAS	60	$\simeq 0.5 \times 10^{-18}$	—	—	—
HSC J160107+550720	FOCAS	60	$\simeq 0.3 \times 10^{-18}$	—	—	—
HSC J233408+004403	FOCAS	60	$\simeq 0.3 \times 10^{-18}$	MOSFIRE	120	$\simeq 0.8 \times 10^{-18}$
HSC J021835-042321 ^a	—	—	—	MOSFIRE	120	$\simeq 1.5 \times 10^{-18}$
HSC J233454+003603	FOCAS	60	$\simeq 1.0 \times 10^{-18}$	MOSFIRE	120	$\simeq 0.6 \times 10^{-18}$
HSC J021752-053511	FOCAS	60	$\simeq 0.1 \times 10^{-18}$	—	—	—
HSC J232558+002557	FOCAS	60	$\simeq 0.2 \times 10^{-18}$	—	—	—
HSC J022001-051637	LDSS3	45	$\simeq 0.3 \times 10^{-18}$	—	—	—

(1) Object ID. Sorted by the NB magnitude.

(2) Instrument for optical spectroscopy.

(3) Integration time for optical spectroscopy.

(4) The 1σ line flux sensitivity near Ly α emission lines.

(5) Instrument for NIR spectroscopy.

(6) Integration time for NIR spectroscopy.

(7) Average values of the 1σ line flux sensitivity at the expected wavelengths of C IV, He II, and O III].^a Spectroscopically confirmed with Magellan/IMACS. See Section 3.1.3.**Table 2.** Number of Spectroscopically Confirmed HSC LAEs at $z \simeq 5.7 - 6.6$.

Sample	$N_{\text{LAE,spec}}$	Spec. Obs. or Sample
(1)	(2)	(3)
Bright ($NB < 24$)	13	FOCAS, LDSS3
Bright ($NB < 24$)	8	IMACS
Bright ($NB < 24$)	7	Literature ^a
Faint ($NB > 24$) ^b	68	LDSS3, IMACS, Literature ^a
Total	96	—

(1) LAE sample. (2) Number of spectroscopically confirmed LAEs. (3) Instruments for observations and spectroscopic samples.

^a Murayama et al. (2007); Taniguchi et al. (2009); Ouchi et al. (2008); Ouchi et al. (2010); Mallery et al. (2012); Sobral et al. (2015); Hu et al. (2016).^b See Tables 8 and 9.**Table 3.** Contamination Rates in the HSC LAE Candidates

Redshift	N_{obs}	$N_{\text{low-z}}$	f_{contami}	Spec. Obs.
(1)	(2)	(3)	(4)	(5)
Bright ($NB < 24$)				
6.6	12	4	0.33	FOCAS ^a , LDSS3 ^a
5.7	6	1	0.17	FOCAS ^a , LDSS3 ^a
All				
6.6	28	4	0.14	FOCAS ^a , LDSS3 ^{a,b} , IMACS ^c
5.7	53	4	0.08	FOCAS ^a , LDSS3 ^a , IMACS ^c

(1) Redshift of the LAE sample. (2) Number of spectroscopically observed HSC LAEs. (3) Number of low- z contaminants. (4) Contamination rates. (5) Spectroscopic follow-up observations. Only for the observations whose N_{obs} and $N_{\text{low-z}}$ are found.^a This study.^b Y. Harikane et al. in preparation.^c R. Higuchi in preparation.

extended or not in Ly α based on our measurements of isophotal areas, A_{iso} (see Shibuya et al. 2017). We find that only 5 out of the 28 bright LAEs show the spatially extended Ly α emission. The A_{iso} measurements indicate that Ly α emission of the bright LAEs is typically compact.

4.2 Ly α Line Width

To quantify the Ly α line profiles, we measure the FWHM velocity width, ΔV_{FWHM} . We fit the symmetric Gaussian profile

to the Ly α emission lines, and obtain the observed FWHM velocity width, ΔV_{obs} in the same manner as that in Ouchi et al. (2010) for consistency. We correct for the instrumental broadening of line profile, and obtain ΔV_{FWHM} by $\Delta V_{\text{FWHM}} = \sqrt{\Delta V_{\text{obs}}^2 - \Delta V_{\text{inst}}^2}$, where ΔV_{obs} and ΔV_{inst} are FWHM velocity widths for the observed Ly α lines and the instrumental resolution, respectively. We use the uncertainties in the χ^2 minimization fitting as the ΔV_{FWHM} errors. The ΔV_{FWHM} values

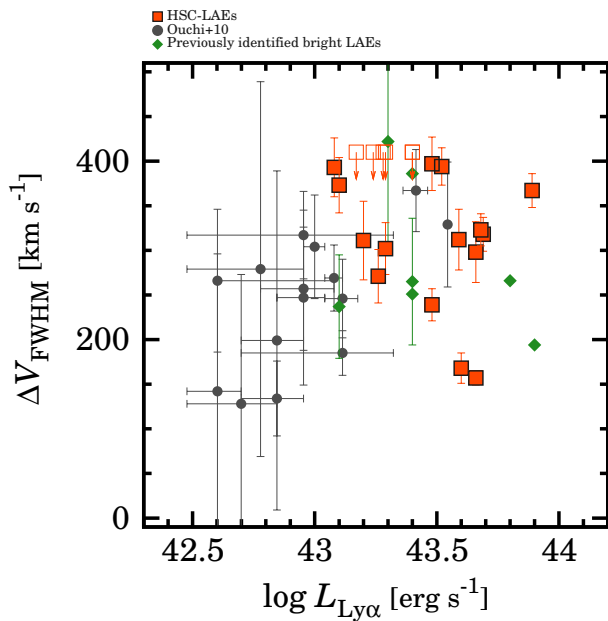


Fig. 5. Ly α line FWHM as a function of Ly α luminosity. The red filled and open squares indicate our bright LAEs whose Ly α emission line is spectroscopically resolved and not resolved, respectively. The green filled diamonds denote bright LAEs which have been previously confirmed (Hu et al. 2016; Sobral et al. 2015; Ouchi et al. 2009; Mallery et al. 2012). The black circles present faint $z \simeq 6.6$ LAEs with $\log L_{\text{Ly}\alpha}/[\text{erg s}^{-1}] \lesssim 43$ in Ouchi et al. (2010).

are listed in Table 6.

Figure 5 presents ΔV_{FWHM} as a function of $L_{\text{Ly}\alpha}$. We find that the bright LAEs have $\Delta V_{\text{FWHM}} \simeq 200 - 400 \text{ km s}^{-1}$ similar to $z \simeq 6$ faint LAEs with $\log L_{\text{Ly}\alpha}/[\text{erg s}^{-1}] \lesssim 43$ (Ouchi et al. 2010). The narrow Ly α emission lines of $\Delta V \simeq 200 - 400 \text{ km s}^{-1}$ indicate that the bright LAEs are not broad-line AGNs.

To quantify the relation between ΔV_{FWHM} and $L_{\text{Ly}\alpha}$ in Figure 5, we carry out Spearman rank correlation tests. In this test, we find a marginal correlation at the $\simeq 1.7\sigma$ significance level, possibly suggesting that ΔV_{FWHM} increases with increasing $L_{\text{Ly}\alpha}$.

4.3 X-ray, Mid-IR, and Radio Detectability

We check X-ray, mid-IR (MIR), and radio data to investigate whether the bright LAEs have a signature of AGN activities. Such X-ray, MIR, and radio data are available in the UD fields, UD-COSMOS and UD-SXDS. In UD-COSMOS, an object (i.e. HSC J100334+024546) is covered by MIR and radio data. In UD-SXDS, all the 10 objects are observed in X-ray, MIR, and radio. For the X-ray data, we use the *XMM-Newton* source catalog whose sensitivity limit is $f_{0.5-2\text{keV}} = 6 \times 10^{-16} \text{ erg cm}^{-2} \text{ s}^{-1}$ (Ueda et al. 2008). For the MIR data, we use *Spitzer*/MIPS $24\mu\text{m}$ source catalogs for UD-COSMOS (Sanders et al. 2007) and UD-SXDS (the SpUDS survey, PI: J. Dunlop). These *Spitzer*/MIPS $24\mu\text{m}$ images reach 5σ sensitivity limits of 21.2

mag and 18.0 mag in UD-COSMOS and UD-SXDS, respectively. For the radio data, we check the Very Large Array (VLA) 1.4 GHz source catalogs of Schinnerer et al. (2007) for UD-COSMOS, and Simpson et al. (2006) for UD-SXDS. The typical r.m.s noise level of the VLA data is $f_{1.4\text{GHz}} \simeq 10 \mu\text{Jy beam}^{-1}$.

We find that there are no counterparts in the X-ray, MIR, and radio data. The no X-ray, MIR, and radio counterparts indicate that there is no clear signature of AGN activities based on the multi-wavelength data. By considering the typical SED of AGNs (e.g., Elvis et al. 1994; Telfer et al. 2002; Richards et al. 2003), the rest-frame UV luminosity of LAEs, and the sensitivity limits of these multi-wavelength data, we rule out, at least, the possibility that the LAEs have radio-loud AGNs.

4.4 UV Nebular Line Flux

Here we investigate whether the rest-frame UV-nebular lines of N v $\lambda\lambda 1238, 1240$, C iv $\lambda\lambda 1548, 1550$, He ii $\lambda 1640$, and O iii] $\lambda\lambda 1661, 1666$ are detected from the bright LAEs. First, we check the detectability of N v emission line which is a coarse indicator of AGN presence. The wavelengths of N v are covered by the FOCAS, LDSS3, and IMACS optical spectra for both of the $z \simeq 6.6$ and $z \simeq 5.7$ LAE samples. In order to estimate the flux limits, we sample the 1D spectra in $\simeq 10 \text{ \AA}$ bins (comparable to the Ly α line FWHM) around the expected wavelengths of N v. We then obtain the flux limit by using the flux distribution over a $\pm 50 \text{ \AA}$ range of the expected wavelengths of N v. We find that there are no N v emission lines for all the 21 bright LAEs. The 2σ flux limits for the N v emission lines are listed in Table 7. The line flux ratio of N v to Ly α is typically $f_{\text{NV}}/f_{\text{Ly}\alpha} \lesssim 10\%$.

Next, we search for the UV-nebular emission lines of C iv, He ii, and O iii] for the seven bright LAEs whose NIR spectra are obtained (Section 3.2). Figure 6 presents the NIR spectra for the seven LAEs. Even in the deep NIR spectra with a 3σ line flux sensitivity limit of $\simeq 2 \times 10^{-18} \text{ erg s}^{-1} \text{ cm}^{-2}$, we find no significant emission features at the expected wavelengths of redshifted He ii, C iv, and O iii] lines, except for a tentative C iv detection from a $z \simeq 5.7$ LAE, HSC J233408+004403 (see below in this section). The flux limits for the C iv, He ii, and O iii] emission lines are estimated in the same manner as that for N v. To estimate the detection limits, we assume a single emission line even for the C iv and O iii] doublets which are resolved in the spectral resolution of MOSFIRE and nuMOIRCS. The 2σ flux limits for individual UV-nebular emission lines are listed in Table 7.

Our deep NIR spectroscopy indicates that there are no significant detections of the UV-nebular emission lines for bright LAEs. By our visual inspections for the NIR spectra, we find a tentative detection of C iv $\lambda 1550$ emission line from the bright-

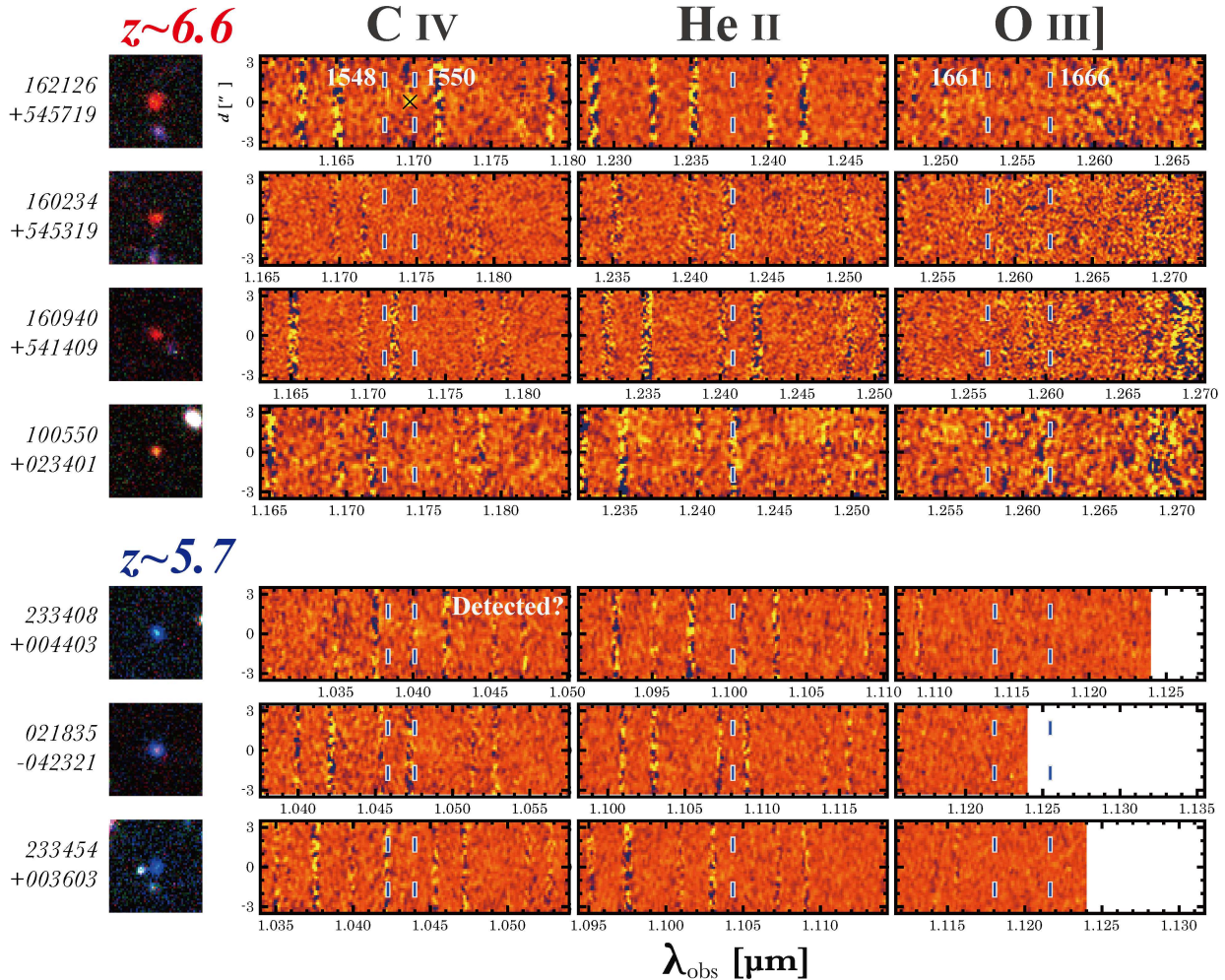


Fig. 6. NIR spectra for the bright LAEs at $z \simeq 6.6$ (the upper four spectra) and $\simeq 5.7$ (the lower three spectra). The left figures indicate the three-color composite images of the bright LAEs. The blue ticks denote the C IV (left), He II (center), and O III (right) wavelengths which are expected from the redshift of Ly α emission line. For HSC J162126+545719, the emission feature near the expected C IV $\lambda 1550$ wavelength is likely to be a residual of the sky subtraction, which is marked by a black cross. A C IV $\lambda 1550$ emission line is tentatively detected in the spectrum of HSC J233408+004403 (see Figure 7), which is discussed in Section 5.3.

est LAE in the $z \simeq 5.7$ sample, HSC J233408+004403. Figure 7 shows the NIR spectra around the wavelengths of the C IV emission line doublet for HSC J233408+004403. The C IV $\lambda 1550$ emission line is tentatively detected at the $\simeq 4 - 9\sigma$ significance level. The significance of the line detection depends on the wavelength range of flux integration. We also identify two negative C IV $\lambda 1550$ emission lines which could be originated from the $\pm 3''$ slit dithering processes in the MOSFIRE observation. Moreover, the tentative C IV $\lambda 1550$ detection might explain a possible magnitude excess in the y -band covering the C IV wavelength (see Figure 3). The line flux is $\simeq 1.2 \times 10^{-17}$ erg cm $^{-2}$ s $^{-1}$. The emission line has a velocity width of $\Delta V_{\text{FWHM}} \simeq 50$ km s $^{-1}$ which is marginally resolved in the MOSFIRE spectral resolution. We do not detect the C IV $\lambda 1548$ component of the C IV doublet from HSC J233408+004403. The single C IV emission line at $\lambda_{\text{rest}} \simeq 1550$ Å may be formed

by a combination of absorption and emission lines that could be originated from stellar winds and ISM. Such a C IV line profile has been found for $z \simeq 1 - 3$ galaxies (e.g., Shapley et al. 2003; Erb et al. 2010; Du et al. 2016). We discuss the emission line properties of the C IV emitter in Section 5.3.

4.5 Re-analysis of CR7 Spectra

We investigate the VLT/X-SHOOTER spectrum of CR7 whose 6σ detection of He II is claimed by Sobral et al. (2015). Two individuals of the authors in this paper and the ESO-archive service re-analyze the VLT/X-SHOOTER data that are used in the study of Sobral et al. (2015). We apply three methods to our re-analysis: (1) reducing the raw data with the X-SHOOTER reduction pipeline ESO REFLEX (*Pipeline*), (2) stacking of each 2D 1-exposure spectrum reduced by ESO (*ESO 2D*), and (3)

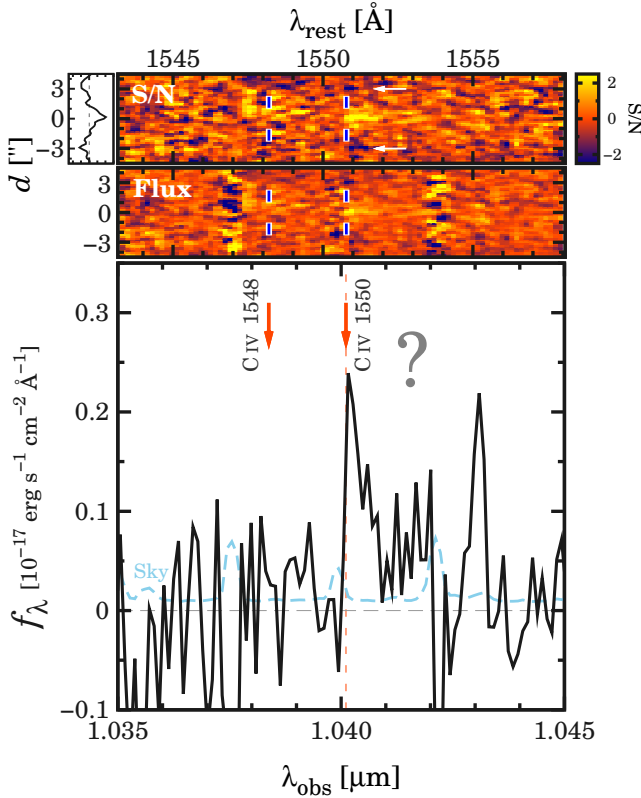


Fig. 7. Tentative detection of a C IV $\lambda 1550$ emission line for HSC J233408+004403. The 2D spectra in the top and middle panels present the S/N and flux maps, respectively. The bottom panel shows the 1D spectrum of the flux map. The white arrows indicate the expected positions of the negative C IV $\lambda 1550$ emission lines which are produced in the $\pm 3''$ slit dithering processes. The top-left panel depicts the 1D S/N spectrum along the spatial direction at the tentative C IV $\lambda 1550$ emission line. The blue ticks and the red arrows indicate the C IV $\lambda 1548$ and C IV $\lambda 1550$ wavelengths expected from the Ly α emission line (i.e. $z_{\text{Ly}\alpha} = 5.707$). The cyan dashed line present the OH sky emission. The C IV $\lambda 1550$ emission line is tentatively detected at a significance level of $\simeq 4 - 9$.

stacking of each 1D 1-exposure spectrum reduced by ESO (*ESO ID*). We smooth our reduced X-SHOOTER spectra with a kernel of $\simeq 0.4 \text{ \AA}$ width which corresponds to that of Sobral et al. (2015).

Figure 8 presents our reduced X-SHOOTER data of the optical (the left panel) and NIR (the right panel) arms for CR7 with the 1D spectrum obtained by Sobral et al. (2015). As shown in the left panel of Figure 8, we clearly identify a Ly α emission line at $\lambda_{\text{rest}} = 1216 \text{ \AA}$. The Ly α line profiles of our data are in good agreement with that of the Sobral et al.'s optical spectrum. However, we find no signal at $\lambda_{\text{rest}} = 1640 \text{ \AA}$ where Sobral et al. (2015) find the emission line feature (the right panel of Figure 8). The detection significance is $< 1\sigma$ at $\lambda_{\text{rest}} = 1640 \text{ \AA}$ in our NIR spectra. Instead, our NIR spectra show a feature of two possible peaks at $\lambda_{\text{rest}} = 1643 \text{ \AA}$ which is redder than the He II wavelength of Sobral et al. (2015) by $\Delta\lambda_{\text{rest}} \simeq 3 \text{ \AA}$ corresponding to the redshift difference of $\Delta z = 0.01$. If we regard the two

possible peaks as He II, we obtain a detection significance of $\simeq 1.8\sigma$. This significance value is inconsistent with the 6σ detection of Sobral et al. (2015). Moreover, the red component of the two possible peaks appears to be made by sky subtraction residuals, as shown in the panel (a) of Figure 8. In the case that this red component is masked for the line flux calculation, the detection significance decreases to $\simeq 1.1\sigma$. To obtain all the values of detection significance and noise levels, we use OH sky line-free regions.

In our careful re-analysis for the X-SHOOTER data, we find that no He II signal of CR7 is detected. The no He II detection supports weak UV-nebular lines of the bright LAEs even for CR7. Based on our S/N -based re-analysis and the flux error from Sobral et al. (2015), we obtain the 3σ upper limits of He II flux and EW for CR7, $f_{\text{HeII}} < 2.1 \times 10^{-17} \text{ erg s}^{-1} \text{ cm}^{-2}$ and $EW_{\text{HeII}} < 60 \text{ \AA}$, respectively.³

4.6 Line Flux Ratios

Figure 9 represents the line flux ratios of He II/Ly α and C IV/Ly α for our bright LAEs and several Ly α -emitting populations such as $z \simeq 6 - 7$ LAEs (Zabl et al. 2015; Kashikawa et al. 2012; Nagao et al. 2005), spatially extended Ly α blobs (LABs; Dey et al. 2005; Prescott et al. 2009; Prescott et al. 2013; Arrigoni Battaia et al. 2015), $z \simeq 2 - 3$ metal-poor and star-forming galaxies (Shapley et al. 2003; Erb et al. 2010), AGNs, QSOs, and radio galaxies (Villar-Martín et al. 2007; Heckman et al. 1991; Humphrey et al. 2013; Borisova et al. 2016).⁴ We add CR7 with our updated He II/Ly α constraint in Section 4.5. The UV-nebular lines of C IV, He II, and O III] are not detected from all of our 7 bright LAEs even for CR7 except for a tentative C IV detection (Section 5.3). Albeit with only upper limits on the line flux ratios, we find that our bright LAEs typically have flux ratios of He II/Ly α and C IV/Ly α lower than those of AGNs, QSOs, radio galaxies, and LABs, but similar to those of star forming galaxies in Shapley et al. (2003) and Erb et al. (2010). Interestingly, the UV-nebular lines are extremely faint for several of our bright LAEs. For such objects, the flux ratio of the UV-nebular lines relative to Ly α , i.e. $f_{\text{UV line}}/f_{\text{Ly}\alpha}$, is below the order of 1 %.

³ Recently, the He II/Ly α line flux ratio for CR7 has been updated based on the flux recalibration of the X-SHOOTER spectrum in Matthee et al. (2017) and Sobral et al. (2017).

⁴ Note that the C IV doublet is not spectroscopically resolved for some of the previous studies. The flux upper limit for such an unresolved C IV doublet would be higher than that of resolved C IV lines. But, the systematics of the C IV flux upper limits are as small as $\simeq 0.15$ dex in a flux ratio of $\log(\text{Ly}\alpha/\text{CIV})$, which could not affect the main conclusion.

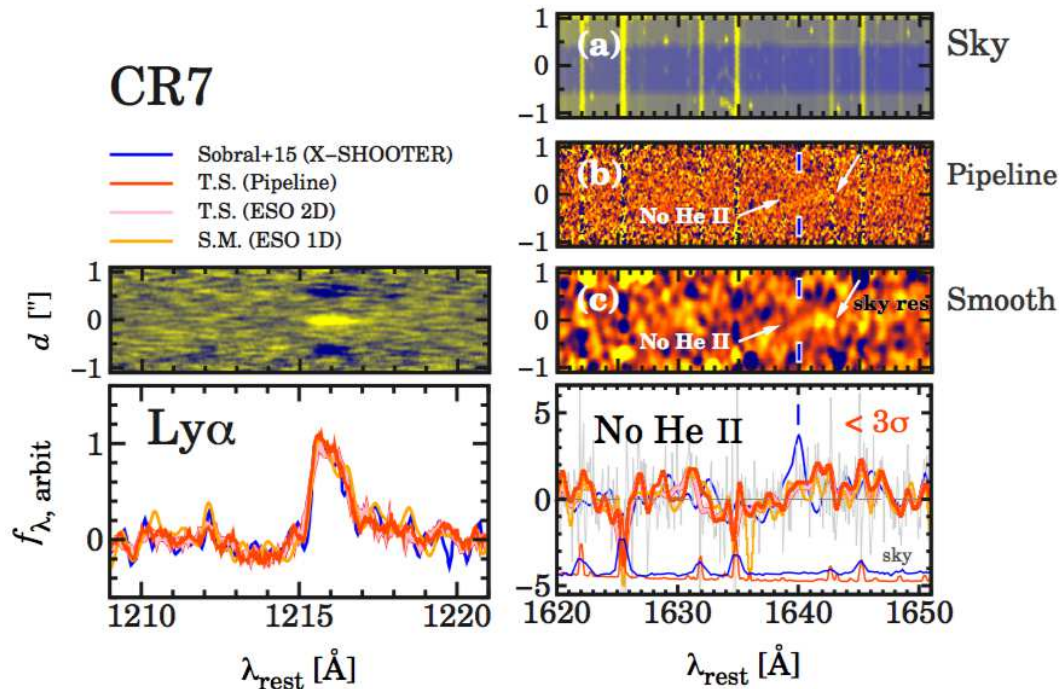


Fig. 8. Re-analyzed VLT/X-SHOOTER spectra of CR7. The left and right panels denote the VIS and NIR arms of the X-SHOOTER spectra. The blue lines indicate the X-SHOOTER spectra in Sobral et al. (2015). The red, magenta, and orange lines depict spectra obtained from (1) reducing the raw data with the X-SHOOTER reduction pipeline `ESO REFLEX (Pipeline)`, (2) stacking of each 2D 1-exposure spectrum reduced by ESO (`ESO 2D`), and (3) stacking of each 1D 1-exposure spectrum reduced by ESO (`ESO 1D`), respectively. These lines have been smoothed with a kernel of $\simeq 0.4 \text{ \AA}$ width which is similar to that of Sobral et al. (2015). The gray lines present the un-smoothed spectrum obtained from our data reduction with `ESO REFLEX`. The thin blue and red lines indicate sky OH lines in Sobral et al. (2015) and our re-analyzed data, respectively. The top-left panels show the 2D spectrum of the X-SHOOTER VIS arm. The top-right panels indicate (a) sky OH line, (b) un-smoothed and (c) smoothed 2D spectra, all of which are obtained from our data reduction with `ESO REFLEX`. The feature at $\lambda_{\text{rest}} = 1643 \text{ \AA}$ appears to be made by sky subtraction residuals. The blue ticks indicate the position of He II whose detection is claimed by Sobral et al. (2015). See Section 4.5 for more details.

5 Discussion

5.1 Properties of Bright LAEs at $z \simeq 6$

We summarize the properties of the bright $z \simeq 6 - 7$ LAEs which have been revealed in our statistical study (Section 4).

- The $\text{Ly}\alpha$ equivalent widths, $EW_{0, \text{Ly}\alpha}$, range from $\simeq 10 \text{ \AA}$ to $\simeq 300 \text{ \AA}$.
- The $\text{Ly}\alpha$ line widths are $\simeq 200 - 400 \text{ km s}^{-1}$.
- There are no detections of X-ray, MIR, and radio emission.
- The N V emission line is not detected down to a N V/ $\text{Ly}\alpha$ flux ratio of $\simeq 10\%$.
- Most of the bright LAEs have the compact $\text{Ly}\alpha$ emission. Only 5 objects out of the 28 bright LAEs show $\text{Ly}\alpha$ emission which are significantly extended compared to the PSF FWHM size of $\simeq 0''.7$ in the ground-based HSC NB images.
- The UV-nebular lines of C IV, He II, and O III] are not detected from all of our 7 bright LAEs even for CR7 except for a tentative C IV detection (Section 5.3). The flux ratio of the UV-nebular lines relative to $\text{Ly}\alpha$ is $f_{\text{UV line}}/f_{\text{Ly}\alpha} \lesssim 1 - 10\%$.

Here we discuss the physical origins of bright LAEs with $\log L_{\text{Ly}\alpha}/[\text{erg s}^{-1}] \simeq 43 - 44$. The bright $\text{Ly}\alpha$ emission could

be reproduced by several mechanisms: (1) gas photo-ionization by a hidden AGN, (2) strong UV radiation from Pop III stellar populations, (3) gas shock heating by strong outflows from central galaxies, and (4) intense starbursts by galaxy mergers.

Firstly, we discuss the possibility of AGNs. For $z \simeq 2$, Konno et al. (2016) have identified a significant hump of LAE number density at the $\text{Ly}\alpha$ LF bright-end of $\log L_{\text{Ly}\alpha}/[\text{erg s}^{-1}] \gtrsim 43.4$. All of the $z \simeq 2$ LAEs in the bright-end hump are detected in X-ray, UV, or radio data, suggesting that the bright $\text{Ly}\alpha$ emission is produced by the central AGN activity. Similarly, there is a possibility that AGNs enhance the $\text{Ly}\alpha$ luminosity for bright LAEs at $z \simeq 6 - 7$. However, we find no clear signatures of AGNs according to the narrow $\text{Ly}\alpha$ line widths of $\lesssim 400 \text{ km s}^{-1}$ and no detections of N V line, X-ray, MIR, nor radio emission. Thus, the bright LAEs at $z \simeq 5.7 - 6.6$ do not host broad-line AGNs, regardless of the bright $\text{Ly}\alpha$ emission.

Secondly, we discuss the possibility of Pop III stellar populations. There is a possibility that strong UV radiation from Pop III stellar populations enhance the $\text{Ly}\alpha$ luminosity (e.g., Schaerer 2002). In our deep NIR spectroscopy, we find that there are no detections of He II emission line from CR7, Himiko, nor our 7 bright LAEs which are observed with NIR

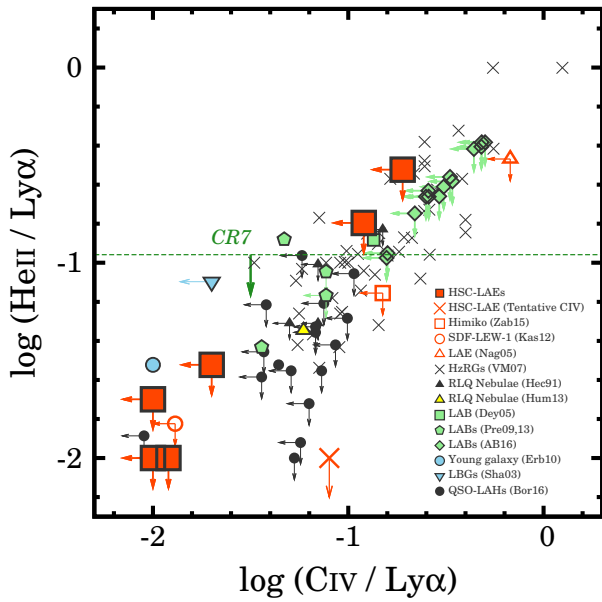


Fig. 9. Flux ratios of UV-nebuluar emission lines, $\text{He II}/\text{Ly}\alpha$ vs $\text{C IV}/\text{Ly}\alpha$. The red filled squares indicate our bright LAEs. The red cross denotes our bright LAE whose C IV emission line is tentatively detected (see Section 5.3). The red open symbols indicate $z \gtrsim 6$ LAEs (red open square: Himiko in Zabl et al. 2015; red open circle: SDF-LEW-1 in Kashikawa et al. 2012; SDF J132440.6+273607: Nagao et al. 2005). The green arrow and dashed line are our $\text{He II}/\text{Ly}\alpha$ constraint for CR7 (see Section 4.5). The green filled symbols represent LABs (green filled square: Dey et al. 2005; green filled pentagons: Prescott et al. 2009; Prescott et al. 2013; green filled diamonds: Arrigoni Battaia et al. 2015). The cyan filled symbols present $z \simeq 2-3$ star-forming galaxies (cyan filled inverse-triangle: Shapley et al. 2003; cyan filled circle Erb et al. 2010). The black and yellow symbols indicate AGNs, QSOs, and radio galaxies (black crosses: Villar-Martín et al. 2007; black filled triangles: Heckman et al. 1991; yellow filled triangles: Humphrey et al. 2013; black filled circles: Borisova et al. 2016). The data points without a UV-nebuluar line detection indicate 2σ upper limits.

spectrographs. Moreover, the $\text{Ly}\alpha$ EW does not significantly exceed the $EW_{0,\text{Ly}\alpha}$ value of 240 \AA for the bright LAEs. The no He II detection and the small $EW_{0,\text{Ly}\alpha}$ values might indicate that the bright LAEs do not host Pop III stellar populations. The no Pop III stellar populations in bright LAEs might be supported by theoretical studies. According to a recent theoretical study of Yajima & Khochfar (2017), Pop III-dominated galaxies at $z \simeq 7$ have a $\text{Ly}\alpha$ luminosity of $L_{\text{Ly}\alpha} \simeq 3.0 \times 10^{42} - 2.1 \times 10^{43} \text{ erg s}^{-1}$ which is slightly lower than that of our bright LAEs. However, we cannot obtain the conclusion that Pop III stellar populations exist in bright LAEs from the current data of He II measurements. The detectability of He II emission line would largely depend on the stellar initial mass function of galaxies (see Section 5.4). To examine whether bright LAEs host Pop III stellar populations, we require NIR spectra whose depth is $\simeq 10\times$ deeper than the current NIR flux limits.

Thirdly, we discuss the possibility that strong outflows enhance the $\text{Ly}\alpha$ luminosity (e.g., Dijkstra & Wyithe 2010). If strong outflows exist, expelling high velocity clouds could make

$\text{Ly}\alpha$ lines broad and $\text{Ly}\alpha$ emission spatially extended. Our spectroscopy reveals that bright LAEs have a narrow $\text{Ly}\alpha$ emission line of $\Delta V_{\text{FWHM}} \lesssim 400 \text{ km s}^{-1}$. Our A_{iso} measurements also indicate that most of our bright LAEs show the spatially compact $\text{Ly}\alpha$ emission (see Section 4.1 and Table 6). The narrow $\text{Ly}\alpha$ line width and the spatially compact $\text{Ly}\alpha$ emission might suggest no strong gaseous outflow from the bright LAEs. However, we cannot conclude the presence of gaseous outflow based on our current data of optical spectra and NB images due to the resonance nature of $\text{Ly}\alpha$ photons. To investigate the presence of gaseous outflow, we have to directly measure velocity shifts of low-ionization metal lines with deep NIR spectra for the rest-frame UV continuum emission (e.g., Shibuya et al. 2014b; Erb et al. 2014; Erb 2015; Trainor et al. 2015; Sugahara et al. 2017).

Finally, we discuss the possibility that intense starbursts driven by galaxy mergers produce the large $\text{Ly}\alpha$ luminosity. High spatial resolution imaging observations with *Hubble* WFC3 have been conducted for two objects out of the 28 bright LAEs, Himiko and CR7, both of which show multiple subcomponents in the rest-frame UV continuum emission (Sobral et al. 2015; Ouchi et al. 2013). These multiple subcomponents could be indicative of galaxy mergers (e.g., Jiang et al. 2013; Shibuya et al. 2014a; Kobayashi et al. 2016). However, the galaxy morphology has been unclear for the other 26 bright LAEs in the ground-based and seeing-limited HSC images.

In summary, the physical origins of bright LAEs have still been unknown. At least we can conclude that the bright $\text{Ly}\alpha$ emission is not originated from broad-line AGNs. To obtain the definitive conclusion, we need to systematically perform deep NIR spectroscopy and high spatial resolution imaging observations for a large number of bright LAEs.

5.2 Relation between UV-nebuluar Line EW and UV-continuum Luminosity

Combining samples of our bright LAEs and faint dropouts at $z \simeq 5-7$, we examine the relation between the UV-nebuluar line EWs of C IV , He II , and O III] and UV-continuum luminosity. Figure 10 presents the rest-frame EW of C IV , He II , and O III] as a function of M_{UV} for our bright LAEs and dropouts in literature (e.g., Stark et al. 2015; Mainali et al. 2017; Smit et al. 2017). Here we plot four UV continuum-detected objects out of our 7 bright LAEs whose UV-nebuluar line EW can be constrained. The EW upper limits of our bright LAEs are typically $\lesssim 2.3, 4.0,$ and 2.9 \AA for C IV , He II , and O III] lines, respectively. On the other hand, faint dropouts with $M_{\text{UV}} \gtrsim -20$ emit strongly C IV and O III] lines with $EW_{0,\text{CIV}} \simeq 20 - 40 \text{ \AA}$ and $EW_{0,\text{OIII]}} \simeq 5 - 10 \text{ \AA}$, respectively.

As shown in Figure 10, we find a trend that EWs of C IV and O III] increase towards faint M_{UV} . Such a trend is similar

to recent study results for $z \simeq 2 - 3$ galaxies showing that UV-nebular lines are predominantly detected in faint sources (Stark et al. 2014; Amorín et al. 2017; see also Du et al. 2017 for C III] $\lambda\lambda 1907, 1909$). On the other hand, we do not find a clear trend for He II due to no He II detection from all of our bright LAEs nor $z \simeq 6 - 7$ dropouts. For the clarity of the $EW_{0,CIV}$ and $EW_{0,OIII]$ relations, we fit a quadratic function to the data points of $z \simeq 6 - 7$ dropouts in Stark et al. (2015) and Mainali et al. (2017) and our LAEs. In the fitting, we use the values of EW upper limits for the objects without a UV-nebular line detection. We exclude the LAE with a tentative C IV detection and a $z \simeq 7$ dropout with a weak $EW_{0,OIII]$ constraint in Stark et al. (2015) for the fitting (see Section 5.3). The best-fit quadratic functions are shown in Figure 10.

In contrast to the gravitationally lensed and faint dropouts of Stark et al. (2015), Mainali et al. (2017), and Smit et al. (2017), our bright LAEs have a moderately bright UV magnitude ranging from $M_{UV} \simeq -20$ to $\simeq -22$. The no UV-nebular line detections from the bright sources could suggest that such a high EW_0 value is a characteristic of low-mass galaxies. The high UV-nebular line EW in low-mass galaxies would be due to a hard ionizing spectrum (i.e. ξ_{ion} , the number of LyC photons per UV luminosity; e.g., Nakajima et al. 2016; Bouwens et al. 2016). Moreover, recent studies for $z \simeq 0$ galaxies report that high-ionization UV-nebular lines highly depend on the gas-phase metallicity (e.g., Senchyna et al. 2017). Our possible $EW - M_{UV}$ correlation may also suggest a dependence of UV-nebular line EW on metallicity for $z \simeq 6 - 7$ galaxies via the mass-metallicity relation.

5.3 A Tentative Detection of C IV Emission Line

In this section, we discuss the EW and UV-nebular line ratios for the LAE whose C IV is tentatively detected (Section 4.4). We estimate the C IV EW, $EW_{0,CIV}$, by using the upper limits of the rest-frame UV continuum flux density. We obtain $EW_{0,CIV} \gtrsim 40 \text{ \AA}$, which is comparable to that of a $z \simeq 7$ dropout in Stark et al. (2015). The $EW_{0,CIV}$ value might be too high according to the anti-correlation between EW and UV-continuum luminosity in Section 5.2. However, it should be noted that the UV continuum is not detected for HSC J233408+004403. In the case that the UV magnitude is fainter than $M_{UV} \simeq -21$, the $EW_{0,CIV}$ value would be comparable to the trend that EW_0 is high at a high UV-continuum luminosity.

Assuming that the C IV emission line is detected in HSC J233408+004403, we compare the He II/C IV and O III]/C IV line flux ratios of HSC J233408+004403 with those of star-forming galaxies at $z \simeq 0 - 7$ and AGNs/QSOs (Vanzella et al. 2016; Vanzella et al. 2017; Mainali et al. 2017; Stark et al. 2014; Berg et al. 2016; Alexandroff et al. 2013; Hainline et al. 2011). Figure 11 shows the line flux ratios of He

II/C IV and O III]/C IV for HSC J233408+004403 and star-forming galaxies and AGNs/QSOs. As shown in Figure 11, HSC J233408+004403 has a flux ratio limit of $\log(\text{He II/C IV}) \lesssim -0.9$ similar to that of star-forming galaxies at $z \simeq 7$.

We compare the limits of flux ratios with those of photoionization models of star-forming galaxies and AGNs in Feltre et al. (2016). The comparison suggests that the constraints on the line flux ratios for HSC J233408+004403 are more comparable to star-forming galaxies as ionizing sources than AGNs predicted by the model predictions, supporting the results of no clear signatures of AGN activity in Sections 4.2 and 4.3.

5.4 Spectral Hardness of Bright LAEs

We investigate the spectral hardness of bright LAEs at $z \simeq 6 - 7$ based on the upper limits on the He II/Ly α line flux ratios (Section 4.4). Figure 12 presents the spectral hardness, $Q_{\text{He}^+}/Q_{\text{H}}$, as a function of metallicity, Z , for our bright LAEs and $z \simeq 6 - 7$ LAEs in previous studies (Himiko in Zabl et al. 2015; SDF-LEW-1 in Kashikawa et al. 2012; SDF J132440.6+273607 in Nagao et al. 2005). Here we use $Q_{\text{He}^+}/Q_{\text{H}}$ which is more model-independent than physical quantities of e.g., ξ_{ion} . The $Q_{\text{He}^+}/Q_{\text{H}}$ value is calculated with an equation of

$$\frac{f_{\text{He}}}{f_{\text{Ly}\alpha}} \simeq 0.55 \times \frac{Q(\text{He}^+)}{Q(\text{H})}, \quad (1)$$

where, f_{He} and $f_{\text{Ly}\alpha}$ are the flux of He II and Ly α emission line, respectively. $Q(\text{He}^+)$ and $Q(\text{H})$ are the emitted number of hydrogen and helium ionizing photons, respectively. The $Q_{\text{He}^+}/Q_{\text{H}}$ traces the energy range between 54.4 and 13.6 eV. The factor of 0.55 depends on the electron temperature, here taken to be $T_e = 30 \text{ kK}$ (Schaerer 2002). The $Q(\text{He}^+)/Q(\text{H})$ upper limits calculated from the He II/Ly α line flux ratios (Table 7) ranges from $\log Q(\text{He}^+)/Q(\text{H}) \simeq -0.5$ to $\simeq -1.8$. For five objects of our bright LAEs, we put strong upper limits of $\log Q(\text{He}^+)/Q(\text{H}) \lesssim -1.8$.

Figure 12 also shows the the model spectral hardness predicted from initial mass functions (IMFs) with different stellar mass ranges of $M_* = 1 - 100 M_\odot$, $1 - 500 M_\odot$, and $M_* = 50 - 500 M_\odot$ (Schaerer 2003). The metallicity of bright LAEs has not been constrained yet. If we assume that bright LAEs are extremely metal poor below $\log Z \simeq -8$, top-heavy IMFs with $M_* = 50 - 500 M_\odot$ might be ruled out by our $Q_{\text{He}^+}/Q_{\text{H}}$ constraints for $z \simeq 6 - 7$ LAEs.

6 Summary and Conclusions

We present Ly α and UV-nebular emission line properties of bright LAEs at $z = 6 - 7$ with a luminosity of $\log L_{\text{Ly}\alpha}/[\text{erg s}^{-1}] = 43 - 44$ identified in the 21-deg² area of the SILVERRUSH early sample developed with the

Subaru/HSC survey data (Ouchi et al. 2017; Shibuya et al. 2017).

Our findings are summarized as follows:

- Our optical spectroscopy newly confirm 21 bright LAEs with clear Ly α emission, and contribute to make a spectroscopic sample of 97 LAEs at $z = 6 - 7$ in SILVERRUSH. Our observations enlarge a spectroscopic sample of bright LAEs by a factor of four, allowing for a statistical study on bright LAEs. We find that all the bright LAEs have a narrow Ly α line width of $\lesssim 400 \text{ km s}^{-1}$, and do not have X-ray, MIR, radio, nor N V $\lambda\lambda 1238, 1240$ emissions regardless of the large Ly α luminosity. The narrow Ly α line widths and no X-ray, MIR, radio, nor N V detections suggest that the bright LAEs are not broad-line AGNs.
- From the spectroscopic sample, we select 7 remarkable LAEs as bright as Himiko and CR7 objects, and perform deep Keck/MOSFIRE and Subaru/nuMOIRCS NIR spectroscopy reaching the 3σ -flux limit of $\simeq 2 \times 10^{-18} \text{ erg s}^{-1}$ for the UV-nebular emission lines of He II $\lambda 1640$, C IV $\lambda\lambda 1548, 1550$, and O III] $\lambda\lambda 1661, 1666$. Except for one tentative detection of C IV, we find no strong UV-nebular lines down to the flux limit, placing the upper limits of EW_0 of $\sim 2.3, 4.0$, and 2.9 \AA for He II, C IV, and O III] lines, respectively.
- We investigate the VLT/X-SHOOTER spectrum of CR7 whose 6σ detection of He II is claimed by Sobral et al. (2015). Although two individuals of the authors in this paper and the ESO-archive service carefully re-analyze the X-SHOOTER data that are used in the study of Sobral et al. (2015), no He II signal of CR7 is detected, supportive of weak UV-nebular lines of the bright LAEs even for CR7.
- Spectral properties of these bright LAEs are clearly different from those of faint dropouts at $z \sim 7$ that have strong UV-nebular lines shown in the various studies (e.g., Stark et al. 2015). Comparing these bright LAEs and the faint dropouts, we find anti-correlations between the UV-nebular line EW_0 and UV-continuum luminosity, which are similar to those found at $z \sim 2 - 3$.

The high spatial resolution imaging and deep spectroscopic observations with *Hubble Space Telescope* and *James Webb Space Telescope* will reveal the morphology, ISM properties, and the origins of bright LAEs.

7 Appendix

Tables 8 and 9 present faint $NB > 24$ spectroscopically confirmed HSC LAEs at $z \simeq 6.6$ and $z \simeq 5.7$, respectively. See Section 3.1.4 for more details.

Acknowledgments

We would like to thank Masayuki Akiyama, Mark Dijkstra, Richard Ellis, Tadayuki Kodama, Jorryt Matthee, David Sobral, Daniel Stark, Yuma Sugahara, and Zheng Zheng for useful discussion and comments. We also thank Kentaro Aoki and Ichi Tanaka for their supports of the FOCAS and MOIRCS observations. We thank the anonymous referee for constructive comments and suggestions. This work is based on observations taken by the Subaru Telescope and the Keck telescope which are operated by the National Observatory of Japan. This work was supported by World Premier International Research Center Initiative (WPI Initiative), MEXT, Japan, KAKENHI (15H02064), (23244025), and (21244013) Grant-in-Aid for Scientific Research (A) through Japan Society for the Promotion of Science (JSPS), and an Advanced Leading Graduate Course for Photon Science grant. NK is supported by JSPS grant 15H03645.

The Hyper Suprime-Cam (HSC) collaboration includes the astronomical communities of Japan and Taiwan, and Princeton University. The HSC instrumentation and software were developed by the National Astronomical Observatory of Japan (NAOJ), the Kavli Institute for the Physics and Mathematics of the Universe (Kavli IPMU), the University of Tokyo, the High Energy Accelerator Research Organization (KEK), the Academia Sinica Institute for Astronomy and Astrophysics in Taiwan (ASIAA), and Princeton University. Funding was contributed by the FIRST program from Japanese Cabinet Office, the Ministry of Education, Culture, Sports, Science and Technology (MEXT), the Japan Society for the Promotion of Science (JSPS), Japan Science and Technology Agency (JST), the Toray Science Foundation, NAOJ, Kavli IPMU, KEK, ASIAA, and Princeton University.

This paper makes use of software developed for the Large Synoptic Survey Telescope. We thank the LSST Project for making their code available as free software at <http://dm.lsst.org>

The Pan-STARRS1 Surveys (PS1) have been made possible through contributions of the Institute for Astronomy, the University of Hawaii, the Pan-STARRS Project Office, the Max-Planck Society and its participating institutes, the Max Planck Institute for Astronomy, Heidelberg and the Max Planck Institute for Extraterrestrial Physics, Garching, The Johns Hopkins University, Durham University, the University of Edinburgh, Queen's University Belfast, the Harvard-Smithsonian Center for Astrophysics, the Las Cumbres Observatory Global Telescope Network Incorporated, the National Central University of Taiwan, the Space Telescope Science Institute, the National Aeronautics and Space Administration under Grant No. NNX08AR22G issued through the Planetary Science Division of the NASA Science Mission Directorate, the National Science Foundation under Grant No. AST-1238877, the University of Maryland, and Eotvos Lorand University (ELTE) and the Los Alamos National Laboratory.

References

- Agarwal, B., Johnson, J. L., Zackrisson, E., Labbe, I., van den Bosch, F. C., Natarajan, P., & Khochfar, S. 2016, *MNRAS*, 460, 4003
- Aihara, H., et al. 2017a, arXiv:1702.08449
- . 2017b, arXiv:1704.05858
- Alexandroff, R., et al. 2013, *MNRAS*, 435, 3306
- Amorin, R., et al. 2017, *Nature Astronomy*, 1, 0052
- Arrigoni Battaia, F., Hennawi, J. F., Prochaska, J. X., & Cantalupo, S. 2015, *ApJ*, 809, 163
- Axelrod, T., Kantor, J., Lupton, R. H., & Pierfederici, F. 2010, An open source application framework for astronomical imaging pipelines
- Bagley, M. B., et al. 2017, *ApJ*, 837, 11

- Berg, D. A., Skillman, E. D., Henry, R. B. C., Erb, D. K., & Carigi, L. 2016, *ApJ*, 827, 126
- Borisova, E., et al. 2016, *ApJ*, 831, 39
- Bosch, J., et al. 2017, to be submitted to PASJ
- Bouwens, R. J., Smit, R., Labbé, I., Franx, M., Caruana, J., Oesch, P., Stefanon, M., & Rasappu, N. 2016, *ApJ*, 831, 176
- Bowler, R. A. A., McLure, R. J., Dunlop, J. S., McLeod, D. J., Stanway, E. R., Eldridge, J. J., & Jarvis, M. J. 2016, *ArXiv e-prints*
- Dey, A., et al. 2005, *ApJ*, 629, 654
- Dijkstra, M., Gronke, M., & Sobral, D. 2016, *ApJ*, 823, 74
- Dijkstra, M., & Wyithe, J. S. B. 2010, *MNRAS*, 408, 352
- Dressler, A., et al. 2011, *PASP*, 123, 288
- Du, X., Shapley, A. E., Martin, C. L., & Coil, A. L. 2016, *ApJ*, 829, 64
- . 2017, *ApJ*, 838, 63
- Elvis, M., et al. 1994, *ApJS*, 95, 1
- Erb, D. K. 2015, *Nature*, 523, 169
- Erb, D. K., Pettini, M., Shapley, A. E., Steidel, C. C., Law, D. R., & Reddy, N. A. 2010, *ApJ*, 719, 1168
- Erb, D. K., et al. 2014, *ApJ*, 795, 33
- Fabricius, M., et al. 2016, in *Proc. SPIE*, Vol. 9908, Society of Photo-Optical Instrumentation Engineers (SPIE) Conference Series, 990828
- Feltre, A., Charlot, S., & Gutkin, J. 2016, *MNRAS*, 456, 3354
- Fisher, D. B., et al. 2014, *Nature*, 505, 186
- Hainline, K. N., Shapley, A. E., Greene, J. E., & Steidel, C. C. 2011, *ApJ*, 733, 31
- Hansen, M., & Oh, S. P. 2006, *mras*, 367, 979
- Harikane, Y., et al. 2017, *arXiv:1704.06535*
- Hartwig, T., et al. 2016, *MNRAS*, 462, 2184
- Heckman, T. M., Lehnert, M. D., Miley, G. K., & van Breugel, W. 1991, *ApJ*, 381, 373
- Hu, E. M., Cowie, L. L., Barger, A. J., Capak, P., Kakazu, Y., & Trouille, L. 2010, *ApJ*, 725, 394
- Hu, E. M., Cowie, L. L., Songaila, A., Barger, A. J., Rosenwasser, B., & Wold, I. G. B. 2016, *ApJL*, 825, L7
- Humphrey, A., Binette, L., Villar-Martín, M., Aretxaga, I., & Papaderos, P. 2013, *MNRAS*, 428, 563
- Ichikawa, T., et al. 2006, in *Proc. SPIE*, Vol. 6269, Society of Photo-Optical Instrumentation Engineers (SPIE) Conference Series, 626916
- Ivezic, Z., et al. 2008, *ArXiv e-prints*
- Jiang, L., et al. 2013, *ApJ*, 773, 153
- Johnson, J. L., & Dijkstra, M. 2016, *ArXiv e-prints*
- Jurić, M., et al. 2015, *ArXiv e-prints*
- Kashikawa, N., et al. 2002, *PASJ*, 54, 819
- . 2006, *ApJ*, 648, 7
- . 2011, *ApJ*, 734, 119
- . 2012, *ApJ*, 761, 85
- Kawanomoto, S. 2017, to be submitted to PASJ
- Kobayashi, M. A. R., et al. 2016, *ApJ*, 819, 25
- Kojima, T., Ouchi, M., Nakajima, K., Shibuya, T., Harikane, Y., & Ono, Y. 2016, *ArXiv e-prints*
- Konno, A., Ouchi, M., Nakajima, K., Duval, F., Kusakabe, H., Ono, Y., & Shimasaku, K. 2016, *ApJ*, 823, 20
- Konno, A., et al. 2014, *apj*, 797, 16
- . 2017, *arXiv:1705.01222*
- Magnier, E. A., et al. 2013, *ApJS*, 205, 20
- Mainali, R., Kollmeier, J. A., Stark, D. P., Simcoe, R. A., Walth, G., Newman, A. B., & Miller, D. R. 2017, *ApJL*, 836, L14
- Mallery, R. P., et al. 2012, *ApJ*, 760, 128
- Massey, P., & Gronwall, C. 1990, *ApJ*, 358, 344
- Matthee, J., Sobral, D., Darvish, B., Santos, S., Mobasher, B., Paulino-Afonso, A., Röttgering, H., & Alegre, L. 2017, *ArXiv e-prints*
- Matthee, J., Sobral, D., Santos, S., Röttgering, H., Darvish, B., & Mobasher, B. 2015, *mras*, 451, 400
- McLean, I. S., et al. 2012, in *Proc. SPIE*, Vol. 8446, Ground-based and Airborne Instrumentation for Astronomy IV, 84460J
- Murayama, T., et al. 2007, *ApJS*, 172, 523
- Nagao, T., Motohara, K., Maiolino, R., Marconi, A., Taniguchi, Y., Aoki, K., Ajiki, M., & Shioya, Y. 2005, *ApJL*, 631, L5
- Nakajima, K., Ellis, R. S., Iwata, I., Inoue, A. K., Kusakabe, H., Ouchi, M., & Robertson, B. E. 2016, *ApJL*, 831, L9
- Neufeld, D. A. 1991, *ApJL*, 370, L85
- Oke, J. B., & Gunn, J. E. 1983, *ApJ*, 266, 713
- Ono, Y., et al. 2017, *arXiv:1704.06004*
- Ota, K., et al. 2008, *ApJ*, 677, 12
- Ouchi, M., et al. 2008, *ApJs*, 176, 301
- . 2009, *ApJ*, 696, 1164
- . 2010, *ApJ*, 723, 869
- . 2013, *ApJ*, 778, 102
- . 2017, *arXiv:1704.07455*
- Pacucci, F., Pallottini, A., Ferrara, A., & Gallerani, S. 2017, *MNRAS*, 468, L77
- Pallottini, A., et al. 2015a, *MNRAS*, 453, 2465
- . 2015b, *ArXiv e-prints*
- Planck Collaboration et al. 2016, *A&A*, 594, A13
- Prescott, M. K. M., Dey, A., & Jannuzi, B. T. 2009, *ApJ*, 702, 554
- . 2013, *ApJ*, 762, 38
- Richards, G. T., et al. 2003, *AJ*, 126, 1131
- Sanders, D. B., et al. 2007, *ApJS*, 172, 86
- Schaerer, D. 2002, *A&A*, 382, 28
- . 2003, *A&A*, 397, 527
- Schinnerer, E., et al. 2007, *ApJS*, 172, 46
- Schlafly, E. F., et al. 2012, *ApJ*, 756, 158
- Senchyna, P., et al. 2017, *ArXiv e-prints*
- Shapley, A. E., Steidel, C. C., Pettini, M., & Adelberger, K. L. 2003, *ApJ*, 588, 65
- Shibuya, T., Kashikawa, N., Ota, K., Iye, M., Ouchi, M., Furusawa, H., Shimasaku, K., & Hattori, T. 2012, *ApJ*, 752, 114
- Shibuya, T., Ouchi, M., Nakajima, K., Yuma, S., Hashimoto, T., Shimasaku, K., Mori, M., & Umemura, M. 2014a, *ApJ*, 785, 64
- Shibuya, T., et al. 2014b, *apj*, 788, 74
- . 2017, *ArXiv e-prints:1704.08140*
- Shimasaku, K., et al. 2006, *PASJ*, 58, 313
- Simpson, C., et al. 2006, *MNRAS*, 372, 741
- Smidt, J., Wiggins, B. K., & Johnson, J. L. 2016, *ApJL*, 829, L6
- Smit, R., Swinbank, A. M., Massey, R., Richard, J., Smail, I., & Kneib, J.-P. 2017, *MNRAS*, 467, 3306
- Smith, A., Bromm, V., & Loeb, A. 2016, *MNRAS*, 460, 3143
- Sobral, D., Matthee, J., Darvish, B., Schaerer, D., Mobasher, B., Röttgering, H. J. A., Santos, S., & Hemmati, S. 2015, *apj*, 808, 139
- Sobral, D., et al. 2017, in preparation
- Stark, D. P., et al. 2014, *MNRAS*, 445, 3200
- . 2015, *MNRAS*, 454, 1393
- Sugahara, Y., Ouchi, M., Lin, L., Martin, C. L., Ono, Y., Harikane, Y., Shibuya, T., & Yan, R. 2017, *ArXiv e-prints:1703.01885*

- Suzuki, R., et al. 2008, PASJ, 60, 1347
 Taniguchi, Y., et al. 2005, PASJ, 57, 165
 —. 2009, ApJ, 701, 915
 Telfer, R. C., Zheng, W., Kriss, G. A., & Davidsen, A. F. 2002, ApJ, 565, 773
 Tonry, J. L., et al. 2012, ApJ, 750, 99
 Trainor, R. F., Steidel, C. C., Strom, A. L., & Rudie, G. C. 2015, ApJ, 809, 89
 Ueda, Y., et al. 2008, ApJS, 179, 124
 Vanzella, E., et al. 2016, ApJL, 821, L27
 —. 2017, ApJ, 842, 47
 Villar-Martín, M., Humphrey, A., De Breuck, C., Fosbury, R., Binette, L., & Vernet, J. 2007, MNRAS, 375, 1299
 Visbal, E., Bryan, G. L., & Haiman, Z. 2017, ArXiv e-prints
 Visbal, E., Haiman, Z., & Bryan, G. L. 2016, MNRAS, 460, L59
 Walawender, J., et al. 2016, in Proc. SPIE, Vol. 9908, Society of Photo-Optical Instrumentation Engineers (SPIE) Conference Series, 99082G
 Yajima, H., & Khochfar, S. 2017, MNRAS, 467, L51
 Yuma, S., Ouchi, M., Drake, A. B., Fujimoto, S., Kojima, T., & Sugahara, Y. 2017, ArXiv e-prints
 Zabl, J., Nørgaard-Nielsen, H. U., Fynbo, J. P. U., Laursen, P., Ouchi, M., & Kjærgaard, P. 2015, mnras, 451, 2050

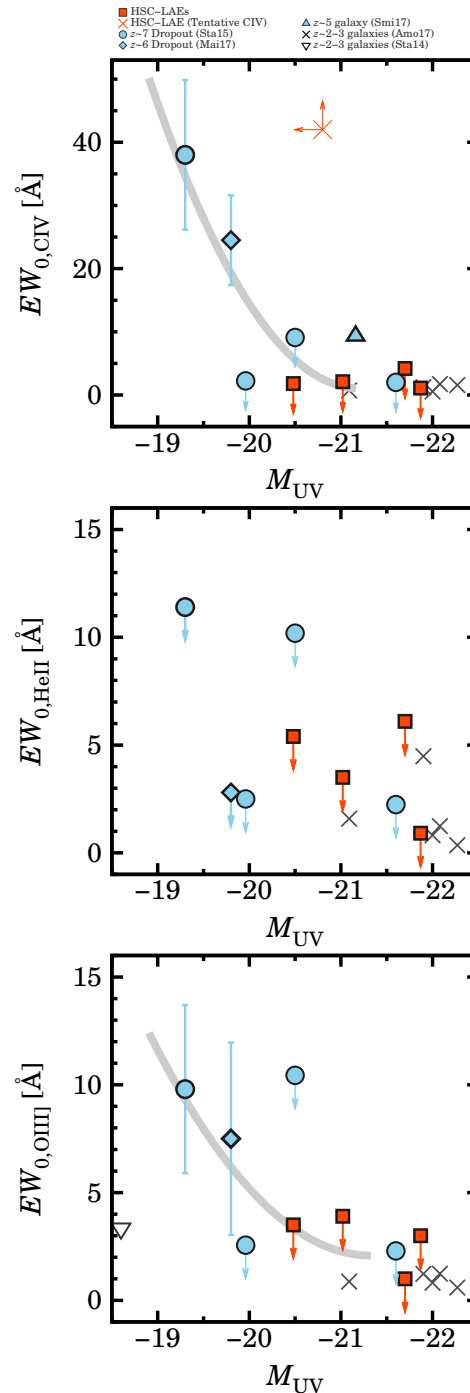


Fig. 10. Line equivalent widths of C IV (top), He II (middle), and O III] (bottom) as a function of UV magnitude, M_{UV} . The red filled squares denote our four bright LAEs with an upper limit of UV-nebular line EW. The red cross represents the LAEs whose C IV emission is tentatively detected. The cyan filled symbols denote high- z dropout galaxies (cyan filled circles: $z \simeq 7$ dropouts in Stark et al. (2015)

; cyan filled diamond: $z \simeq 6$ dropout in Mainali et al. (2017); cyan filled triangle: Smit et al. 2017). The gray symbols indicate $z \simeq 2 - 3$ galaxies (gray crosses: Amorín et al. 2017; gray open inverse-triangle: Stark et al. 2014). The gray curves represent the best-fit quadratic functions to the data points of $z \simeq 6 - 7$ dropouts in Stark et al. 2014 and Mainali et al. (2017) and our LAEs. The data points without a UV-nebular line detection indicate 2σ upper limits.

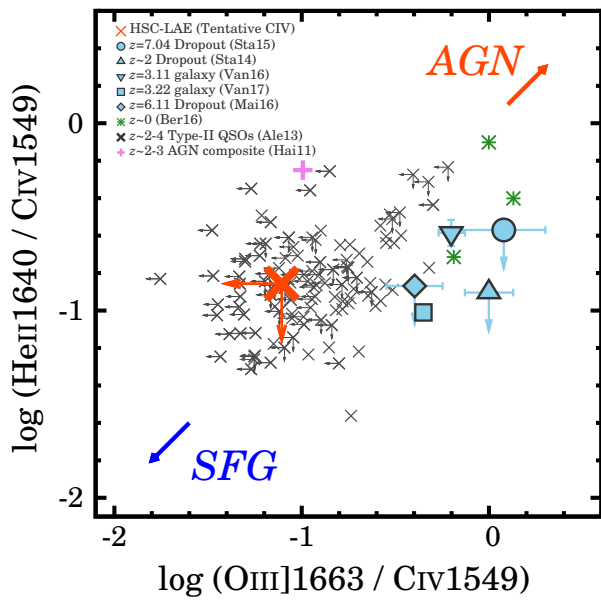


Fig. 11. Flux ratios of UV-nebular emission lines, $\text{He II}/\text{C IV}$ vs $\text{O III]}/\text{C IV}$. The red cross denotes our bright LAE with a tentative C IV emission, HSC J233408+004403. The cyan filled symbols indicate dropouts at $z \simeq 2 - 7$ (cyan squares: Vanzella et al. 2017; cyan filled inverse-triangle: Vanzella et al. 2016; cyan filled diamond; Mainali et al. 2017; cyan filled triangle: Stark et al. 2014). The green asterisks represent $z \simeq 0$ galaxies in Berg et al. (2016). The crosses present QSOs and AGNs (black crosses: $z \simeq 2 - 4$ type-II QSOs in Alexandroff et al. 2013; magenta cross: $z \simeq 2 - 3$ AGN composite in Hainline et al. 2011). The blue and red arrows indicate the SFG and AGN regions predicted by a photoionization model of Feltre et al. (2016), respectively.

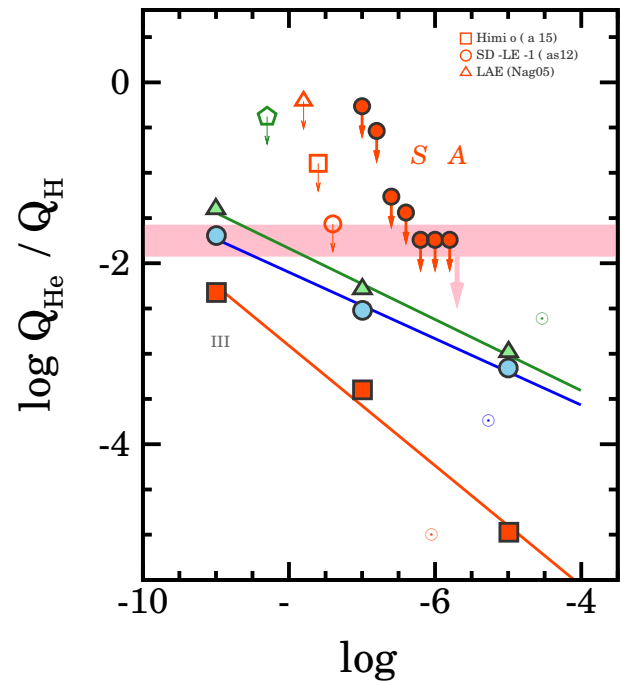


Fig. 12. Spectral hardness of the He^+ ionizing flux, $Q_{\text{He}^+}/Q_{\text{H}}$, as a function of metallicity. The red filled circles represent our bright LAEs. The magenta line indicate the strongest upper limit of our $Q_{\text{He}^+}/Q_{\text{H}}$ estimates. The filled red squares, blue circles, and green triangles with colored lines denote the model predictions of Schaerer (2003) for stellar initial mass functions with mass ranges of $1 - 100 M_{\odot}$, $1 - 500 M_{\odot}$, and $50 - 500 M_{\odot}$, respectively. The open symbols indicate $z \gtrsim 6$ LAEs (red open square: Himiko in Zabl et al. 2015; red open circle: SDF-LEW-1 in Kashikawa et al. 2012; SDF J132440.6+273607: Nagao et al. 2005). The open green pentagon is $Q_{\text{He}^+}/Q_{\text{H}}$ obtained from our $\text{He II}/\text{Ly}\alpha$ constraint for CR7 (see Section 4.5). The metallicity of the observational data points is arbitrary. The data points without a UV-nebular line detection indicate 2σ upper limits.

Table 4. Photometric Properties of Bright LAEs with Spectroscopic Redshifts

Object ID	$\alpha(J2000)$	$\delta(J2000)$	$z_{Ly\alpha}$	NB (mag)	i (mag)	z (mag)	y (mag)
(1)	(2)	(3)	(4)	(5)	(6)	(7)	(8)
<i>NB921</i> ($z \simeq 6.6$)							
HSC J162126+545719	16:21:26.51	+54:57:19.14	6.545	22.33 ± 0.02	> 25.8	23.77 ± 0.18	22.92 ± 0.16
HSC J233125-005216	23:31:25.36	-00:52:16.36	6.559	23.17 ± 0.08	> 26.6	25.34 ± 0.27	24.96 ± 0.37
HSC J160234+545319	16:02:34.77	+54:53:19.95	6.576	23.24 ± 0.05	> 26.4	24.79 ± 0.26	> 24.8
HSC J160940+541409	16:09:40.25	+54:14:09.04	6.564	23.52 ± 0.06	> 26.4	25.45 ± 0.32	> 24.7
HSC J100334+024546	10:03:34.66	+02:45:46.56	6.575	23.61 ± 0.05	> 26.7	25.62 ± 0.27	24.97 ± 0.29
HSC J100550+023401	10:05:50.97	+02:34:01.51	6.573	23.71 ± 0.10	> 26.4	25.15 ± 0.22	> 25.3
HSC J160707+555347	16:07:07.48	+55:53:47.90	6.586	23.86 ± 0.09	> 26.5	25.35 ± 0.32	> 24.8
HSC J160107+550720	16:01:07.45	+55:07:20.63	6.563	23.96 ± 0.12	> 26.4	> 25.5	> 24.4
<i>NB816</i> ($z \simeq 5.7$)							
HSC J233408+004403	23:34:08.79	+00:44:03.78	5.707	22.85 ± 0.04	25.40 ± 0.20	> 25.8	> 25.1
HSC J021835-042321 ^a	02:18:35.94	-04:23:21.62	5.757	23.10 ± 0.06	25.38 ± 0.22	24.93 ± 0.19	25.23 ± 0.56
HSC J233454+003603	23:34:54.95	+00:36:03.99	5.732	23.16 ± 0.05	25.42 ± 0.19	25.60 ± 0.37	24.59 ± 0.28
HSC J021752-053511	02:17:52.63	-05:35:11.78	5.756	23.17 ± 0.05	25.24 ± 0.12	24.50 ± 0.14	24.42 ± 0.20
HSC J021828-051423 ^a	02:18:28.87	-05:14:23.01	5.737	23.57 ± 0.04	26.25 ± 0.22	26.27 ± 0.38	> 25.78
HSC J021724-053309 ^a	02:17:24.02	-05:33:09.61	5.707	23.64 ± 0.08	> 25.8	25.36 ± 0.29	> 25.4
HSC J021859-052916 ^a	02:18:59.92	-05:29:16.81	5.674	23.71 ± 0.06	25.17 ± 0.14	24.05 ± 0.09	24.00 ± 0.17
HSC J021836-053528 ^a	02:18:36.37	-05:35:28.07	5.700	23.75 ± 0.06	25.95 ± 0.22	25.20 ± 0.21	24.88 ± 0.25
HSC J232558+002557	23:25:58.43	+00:25:57.53	5.703	23.78 ± 0.09	25.86 ± 0.22	25.29 ± 0.28	> 24.9
HSC J022001-051637	02:20:01.10	-05:16:37.51	5.708	23.79 ± 0.04	26.04 ± 0.19	25.99 ± 0.30	> 25.8
HSC J021827-044736 ^a	02:18:27.44	-04:47:36.98	5.703	23.80 ± 0.08	26.93 ± 0.38	> 26.3	> 25.8
HSC J021830-051457 ^a	02:18:30.53	-05:14:57.81	5.688	23.83 ± 0.05	25.93 ± 0.17	26.27 ± 0.38	> 25.8
HSC J021624-045516 ^a	02:16:24.70	-04:55:16.55	5.706	23.94 ± 0.06	26.24 ± 0.22	25.67 ± 0.23	> 25.5
Previously identified bright LAEs							
HSC J100235+021213 ^b	10:02:35.38	+02:12:13.96	6.593	23.18 ± 0.03	> 26.9	24.98 ± 0.12	25.29 ± 0.31
HSC J100058+014815 ^c	10:00:58.00	+01:48:15.14	6.604	23.25 ± 0.03	> 26.9	25.12 ± 0.13	24.48 ± 0.16
HSC J021757-050844 ^d	02:17:57.58	-05:08:44.63	6.595	23.50 ± 0.03	> 27.4	25.77 ± 0.20	25.40 ± 0.27
HSC J100124+023145 ^e	10:01:24.79	+02:31:45.38	6.541	23.61 ± 0.03	> 27.0	25.25 ± 0.14	25.64 ± 0.40
HSC J100109+021513 ^f	10:01:09.72	+02:15:13.45	5.712	23.13 ± 0.02	25.77 ± 0.13	25.91 ± 0.21	25.97 ± 0.41
HSC J100129+014929 ^f	10:01:29.07	+01:49:29.81	5.707	23.47 ± 0.02	25.87 ± 0.15	25.27 ± 0.13	25.30 ± 0.28
HSC J100123+015600 ^f	10:01:23.84	+01:56:00.46	5.726	23.94 ± 0.03	26.43 ± 0.25	25.85 ± 0.21	> 25.9

(1) Object ID.

(2) Right ascension.

(3) Declination.

(4) Spectroscopic redshift of Ly α emission line.(5) Total magnitudes of *NB921* and *NB816* for $z \simeq 6.6$ and $z \simeq 5.7$ LAEs, respectively.(6)-(8) Total magnitudes of *i*-, *z*-, and *y*-band.(6)-(8) 2σ limiting magnitudes for undetected bands.^a Spectroscopically confirmed with Magellan/IMACS. See Section 3.1.3.^b COLA1 in Hu et al. (2016).^c CR7 in Sobral et al. (2015).^d Himiko in Ouchi et al. (2009).^e MASOSA in Sobral et al. (2015).^f Spectroscopically confirmed in Mallery et al. (2012).

Table 5. Low- z Contamination Sources

Object ID	$\alpha(J2000)$	$\delta(J2000)$	z_{spec}	NB (mag)	g (mag)	r (mag)	i (mag)	z (mag)	y (mag)
(1)	(2)	(3)	(4)	(5)	(6)	(7)	(8)	(9)	(10)
<i>NB921</i>									
HSC J1001+0229	10:01:44.34	+02:29:09.96	0.840	23.64	26.78	> 26.7	> 26.5	25.10	> 25.0
HSC J0957+0306	09:57:16.07	+03:06:30.31	0.841	23.73	> 27.2	> 26.7	> 26.5	25.15	> 25.0
HSC J1611+5541	16:11:30.34	+55:41:00.39	0.844	23.82	> 27.2	> 26.7	26.37	25.47	> 25.0
HSC J1609+5620	16:09:18.03	+56:20:50.89	0.838	23.96	> 27.2	> 26.7	> 26.5	25.52	> 25.0
<i>NB816</i>									
HSC J2327+0054	23:27:48.16	+00:54:20.84	0.639	23.18	> 27.2	> 26.7	25.31	> 25.8	> 25.0

(1) Object ID.

(2) Right ascension.

(3) Declination.

(4) Spectroscopic redshift.

(5) Total magnitudes of *NB921* and *NB816* for $z \simeq 6.6$ and $z \simeq 5.7$ LAEs, respectively.(6)-(10) Total magnitudes of g -, r -, i -, z -, and y -band.(6)-(10) 2σ limiting magnitudes for undetected bands.

Table 6. Physical Properties of Bright LAEs with Spectroscopic Redshifts

Object ID	$F_{\text{Ly}\alpha}$ ($\text{erg s}^{-1} \text{cm}^{-2}$)	$\log L_{\text{Ly}\alpha}$ (erg s^{-1})	$EW_{0,\text{Ly}\alpha}$ (\AA)	ΔV_{FWHM} (km s^{-1})	M_{UV} (mag)	Extended? ^a
(1)	(2)	(3)	(4)	(5)	(6)	(7)
<i>NB921</i> ($z \simeq 6.6$)						
HSC J162126+545719	16.0 ± 0.12	43.89 ± 0.12	98.6 ± 32.7^i	367 ± 19	-20.48 ± 0.31^i	
HSC J233125-005216	8.20 ± 0.05	43.60 ± 0.15	80.8 ± 33.4	168 ± 17	-21.87 ± 0.37	
HSC J160234+545319	6.74 ± 0.03	43.52 ± 0.002	> 57.3	394 ± 21	> -22.0	
HSC J160940+541409	3.98 ± 0.06	43.29 ± 0.006	> 30.8	302 ± 29	> -22.1	Y
HSC J100334+024546	6.14 ± 0.13	43.48 ± 0.18	61.1 ± 18.9	239 ± 18	-21.87 ± 0.29	
HSC J100550+023401	7.94 ± 0.10	43.59 ± 0.005	> 107.0	312 ± 34	> -21.5	
HSC J160707+555347	6.07 ± 0.05	43.48 ± 0.004	> 51.5	397 ± 30	> -22.0	
HSC J160107+550720	2.45 ± 0.03	43.08 ± 0.005	> 14.4	393 ± 33	> -22.4	
<i>NB816</i> ($z \simeq 5.7$)						
HSC J233408+004403	13.5 ± 0.03	43.68 ± 0.001	> 256.4	323 ± 18	> -20.8	
HSC J021835-042321 ^b	12.5 ± 0.07	43.66 ± 0.08	107.4 ± 21.4	298 ± 34	-21.70 ± 0.19	
HSC J233454+003603	13.6 ± 0.10	43.69 ± 0.14	216.6 ± 88.5	318 ± 19	-21.02 ± 0.37	
HSC J021752-053511	12.7 ± 0.09	43.66 ± 0.06	73.5 ± 10.7	157 ± 8	-22.13 ± 0.14	
HSC J021828-051423 ^b	7.04 ± 0.06	43.40 ± 0.15	207.3 ± 87.2	< 410	-20.35 ± 0.38	
HSC J021724-053309 ^b	5.48 ± 0.02	43.29 ± 0.12	69.5 ± 21.9	< 410	-21.25 ± 0.29	
HSC J021859-052916 ^b	4.55 ± 0.05	43.20 ± 0.04	17.2 ± 1.8	311 ± 44	-22.55 ± 0.09	
HSC J021836-053528 ^b	4.90 ± 0.03	43.24 ± 0.09	53.6 ± 11.8	< 410	-21.41 ± 0.21	
HSC J232558+002557	3.59 ± 0.02	43.10 ± 0.12	42.7 ± 13.1	373 ± 31	-21.32 ± 0.28	
HSC J022001-051637	5.10 ± 0.03	43.26 ± 0.12	115.6 ± 37.1	271 ± 30	-20.62 ± 0.30	
HSC J021827-044736 ^b	5.34 ± 0.05	43.28 ± 0.03	> 160.8	< 410	> -20.3	
HSC J021830-051457 ^b	7.19 ± 0.13	43.40 ± 0.15	210.3 ± 88.8	< 410	-20.34 ± 0.38	
HSC J021624-045516 ^b	4.17 ± 0.03	43.17 ± 0.09	70.5 ± 17.1	< 410	-20.94 ± 0.23	
Previously identified bright LAEs ^c						
HSC J100235+021213 ^d	16.0	43.9	53	194	-21.55 ± 0.31	
HSC J100058+014815 ^e	12.7 ± 0.08	43.8	211	266	-22.37 ± 0.16	Y
HSC J021757-050844 ^f	5.06 ± 0.32	43.4	78	251	-21.44 ± 0.27	Y
HSC J100124+023145 ^g	5.16	43.4	> 206	386	-21.19 ± 0.40	
HSC J100109+021513 ^h	7.32 ± 0.85	43.4	$19.7^{+9.00}_{-7.93}$	265 ± 71	-20.64 ± 0.41	Y
HSC J100129+014929 ^h	5.77 ± 0.61	43.3	$60.9^{+5.89}_{-41.32}$	422 ± 120	-21.31 ± 0.28	Y
HSC J100123+015600 ^h	3.79 ± 0.66	43.1	$11.4^{+8.01}_{-7.32}$	237 ± 58	> -20.72	

(1) Object ID.

(2) Ly α flux in units of $10^{-17} \text{ erg s}^{-1} \text{ cm}^{-2}$.(3) Ly α luminosity.(4) Ly α EW.(5) Velocity FWHM of the Ly α emission line.

(6) Absolute UV magnitude.

(7) Flag of the Ly α spatial extent.^a If the column is Y, the object is spatially extended in Ly α . See Shibuya et al. (2017).^b Spectroscopically confirmed with Magellan/IMACS. See Section 3.1.3.^c Physical quantities in the columns (2)-(5) are obtained from literature.^d COLA1 in Hu et al. (2016).^e CR7 in Sobral et al. (2015).^f Himiko in Ouchi et al. (2009).^g MASOSA in Sobral et al. (2015).^h Spectroscopically confirmed in Mallery et al. (2012).ⁱ These values are calculated from the rest-frame UV continuum emission detected in the spectroscopic data.

Table 7. UV Nebular Emission Lines of Bright LAEs

Object ID (R.A.)	Flux (EW_0) (2σ upper limits)				Line flux ratio relative to $Ly\alpha$			
	N v	C IV	He II	O III]	N v / $Ly\alpha$	C IV / $Ly\alpha$	He II / $Ly\alpha$	O III] / $Ly\alpha$
	$(10^{-17} \text{ erg s}^{-1} \text{ cm}^{-2}) (\text{\AA})$							
(1)	(2)	(3)	(4)	(5)	(6)	(7)	(8)	(9)
J162126	< 0.81(< 7.2)	< 0.13(< 1.8)	< 0.35(< 5.4)	< 0.22(< 3.5)	< 0.05	< 0.01	< 0.02	< 0.01
J233125	< 0.53	< 0.06
J160234	< 0.71	< 0.81	< 1.06	< 1.55	< 0.11	< 0.12	< 0.16	< 0.23
J160940	< 0.56	< 0.77	< 1.20	< 1.95	< 0.14	< 0.19	< 0.30	< 0.49
J100334	< 0.75	< 0.12
J100550	< 0.64(< 6.6)	< 0.07(< 1.1)	< 0.05(0.91)	< 0.16(< 3.0)	< 0.08	< 0.01	< 0.01	< 0.03
J160707	< 0.55	< 0.09
J160107	< 0.66	< 0.27
J233408	< 0.67	1.15(> 42)	< 0.16	< 0.09	< 0.05	0.08 ± 0.008	< 0.01	< 0.01
J021835	< 0.92(< 8.2)	< 0.30(< 4.2)	< 0.39(< 6.1)	< 0.06(< 1.0)	< 0.07	< 0.02	< 0.03	< 0.01
J233454	< 0.64(< 11)	< 0.08(< 2.1)	< 0.12(< 3.5)	< 0.13(< 3.9)	< 0.05	< 0.01	< 0.01	< 0.01
J201752	< 0.70	< 0.06
J021828	< 0.62	< 0.09
J021724	< 0.15	< 0.03
J021859	< 0.59	< 0.13
J021836	< 0.26	< 0.05
J232558	< 0.45	< 0.13
J022001	< 0.72	< 0.14
J021827	< 1.05	< 0.20
J021830	< 1.24	< 0.17
J021624	< 0.43	< 0.10

(1) Object ID.

(2)-(5) Flux and 2σ flux upper limits of the C IV, He II, and O III] emission lines.The number in the parentheses is the EW and 2σ limits of the C IV, He II, and O III] emission lines.(6)-(9) Line flux ratios of the UV-nebular emission lines relative to $Ly\alpha$.

Table 8. Spectroscopically confirmed $z \simeq 6.6$ LAEs with $NB > 24$ mag

Object ID	$\alpha(J2000)$	$\delta(J2000)$	z_{spec}	$NB921$ (mag)	y (mag)	Reference
(1)	(2)	(3)	(4)	(5)	(6)	(7)
<i>NB921</i> ($z \simeq 6.6$)						
HSC J021843–050915	02:18:43.62	–05:09:15.63	6.510	24.33	24.87	Hari
HSC J021703–045619	02:17:03.46	–04:56:19.07	6.589	24.45	25.42	O10
HSC J021827–043507	02:18:27.01	–04:35:07.92	6.511	24.56	25.32	O10
HSC J021844–043636	02:18:44.64	–04:36:36.21	6.621	24.63	27.34	H
HSC J021702–050604	02:17:02.56	–05:06:04.61	6.545	24.64	26.35	O10
HSC J021826–050726	02:18:27.00	–05:07:26.89	6.554	24.69	—	O10
HSC J021819–050900	02:18:19.39	–05:09:00.65	6.563	24.73	26.04	O10
HSC J021654–045556	02:16:54.54	–04:55:56.94	6.617	24.82	25.67	O10

(1) Object ID.

(2) Right ascension.

(3) Declination.

(4) Spectroscopic redshift of Ly α emission line.

(5)-(6) Total magnitudes of *NB921* and *y*-bands.

(7) Reference (O10: Ouchi et al. 2010; Hari: Y. Harikane in prep.; H: R. Higuchi in prep.).

Note that the magnitudes are values directly obtained from the HSC catalog.

Table 9. Spectroscopically confirmed $z \simeq 5.7$ LAEs with $NB > 24$ mag

Object ID	$\alpha(J2000)$	$\delta(J2000)$	z_{spec}	$NB816$ (mag)	z (mag)	Reference
(1)	(2)	(3)	(4)	(5)	(6)	(7)
<i>NB816 ($z \simeq 5.7$)</i>						
HSC J095952+013723	09:59:52.13	+01:37:23.24	5.724	24.07	25.76	M12
HSC J021758-043030	02:17:58.91	-04:30:30.42	5.689	24.07	25.56	H
HSC J095933+024955	09:59:33.44	+02:49:55.92	5.724	24.10	27.25	M12
HSC J021749-052854	02:17:49.11	-05:28:54.17	5.694	24.10	26.77	O08
HSC J021704-052714	02:17:04.30	-05:27:14.30	5.686	24.11	26.29	H
HSC J095952+015005	09:59:52.03	+01:50:05.95	5.744	24.11	25.10	M12
HSC J021737-043943	02:17:37.96	-04:39:43.02	5.7547	24.11	25.63	H
HSC J100015+020056	10:00:15.66	+02:00:56.04	5.718	24.15	26.08	M12
HSC J021734-044558	02:17:34.57	-04:45:58.95	5.702	24.20	25.44	H
HSC J100131+023105	10:01:31.08	+02:31:05.77	5.690	24.23	26.15	M12
HSC J100301+020236	10:03:01.15	+02:02:36.04	5.682	24.24	24.58	M12
HSC J021654-052155	02:16:54.60	-05:21:55.52	5.712	24.24	26.49	H
HSC J021748-053127	02:17:48.46	-05:31:27.02	5.690	24.25	25.67	O08
HSC J100127+023005	10:01:27.77	+02:30:05.83	5.696	24.28	25.61	M12
HSC J021745-052936	02:17:45.24	-05:29:36.01	5.688	24.30	27.26	O08
HSC J021725-050737	02:17:25.90	-05:07:37.59	5.704	24.35	26.21	H
HSC J100208+015444	10:02:08.80	+01:54:44.99	5.676	24.36	25.65	M12
HSC J095954+021039	09:59:54.77	+02:10:39.26	5.662	24.38	25.63	M12
HSC J095950+025406	09:59:50.09	+02:54:06.16	5.726	24.39	26.59	M12
HSC J022013-045109	02:20:13.33	-04:51:09.40	5.744	24.40	25.88	O08
HSC J100126+014430	10:01:26.88	+01:44:30.29	5.686	24.41	25.96	M12
HSC J095919+020322	09:59:19.74	+02:03:22.02	5.704	24.41	26.84	M12
HSC J095954+021516	09:59:54.52	+02:15:16.50	5.688	24.43	25.95	M12
HSC J021849-052235	02:18:49.00	-05:22:35.35	5.719	24.45	25.64	H
HSC J100005+020717	10:00:05.06	+02:07:17.01	5.704	24.46	26.64	M12
HSC J021830-052950	02:18:30.75	-05:29:50.34	5.707	24.46	28.89	H
HSC J100306+014742	10:03:06.13	+01:47:42.69	5.680	24.52	26.54	M12
HSC J021804-052147	02:18:04.17	-05:21:47.25	5.7338	24.54	25.20	H
HSC J100022+024103	10:00:22.51	+02:41:03.25	5.661	24.55	25.34	M12
HSC J021848-051715	02:18:48.23	-05:17:15.45	5.741	24.56	25.45	H
HSC J021750-050203	02:17:50.86	-05:02:03.24	5.708	24.57	26.48	H
HSC J021526-045229	02:15:26.22	-04:52:29.93	5.655	24.62	24.95	H
HSC J021636-044723	02:16:36.44	-04:47:23.68	5.718	24.63	26.57	H
HSC J100030+021714	10:00:30.41	+02:17:14.73	5.695	24.65	26.70	M12
HSC J021558-045301	02:15:58.49	-04:53:01.75	5.718	24.68	26.55	H
HSC J021719-043150	02:17:19.13	-04:31:50.64	5.735	24.68	27.87	H
HSC J021822-042925	02:18:22.91	-04:29:25.89	5.697	24.68	27.65	H
HSC J100131+014320	10:01:31.11	+01:43:20.50	5.728	24.70	26.45	M12
HSC J095944+020050	09:59:44.07	+02:00:50.74	5.688	24.71	26.18	M12
HSC J021709-050329	02:17:09.77	-05:03:29.18	5.709	24.74	26.52	H
HSC J021803-052643	02:18:03.87	-05:26:43.45	5.747	24.75	27.66	H
HSC J100309+015352	10:03:09.81	+01:53:52.36	5.705	24.76	26.61	M12
HSC J021805-052704	02:18:05.17	-05:27:04.06	5.746	24.77	31.43	H
HSC J021739-043837	02:17:39.25	-04:38:37.21	5.720	24.79	27.00	H
HSC J100040+021903	10:00:40.24	+02:19:03.70	5.719	24.81	26.96	M12
HSC J021857-045648	02:18:57.32	-04:56:48.88	5.681	24.85	27.11	H

Table 9. (Continued)

HSC J021745-044129	02:17:45.74	-04:41:29.24	5.674	24.86	27.34	H
HSC J021639-051346	02:16:39.89	-05:13:46.75	5.702	24.87	26.98	H
HSC J021805-052026	02:18:05.28	-05:20:26.90	5.742	24.87	26.10	H
HSC J021755-043251	02:17:55.40	-04:32:51.54	5.691	24.91	27.26	H
HSC J100058+013642	10:00:58.41	+01:36:42.89	5.688	24.91	27.97	M12
HSC J100029+015000	10:00:29.58	+01:50:00.78	5.707	24.97	26.80	M12
HSC J021911-045707	02:19:11.03	-04:57:07.48	5.704	25.00	27.46	H
HSC J021551-045325	02:15:51.34	-04:53:25.44	5.710	25.02	26.76	H
HSC J021625-045237	02:16:25.64	-04:52:37.18	5.728	25.07	—	H
HSC J021751-053003	02:17:51.14	-05:30:03.64	5.712	25.10	26.99	O08
HSC J021628-050103	02:16:28.05	-05:01:03.85	5.692	25.17	27.23	H
HSC J021943-044914	02:19:43.91	-04:49:14.30	5.684	25.17	26.86	H
HSC J100029+024115	10:00:29.13	+02:41:15.70	5.735	25.22	28.30	M12
HSC J100107+015222	10:01:07.35	+01:52:22.88	5.668	25.33	26.42	M12

(1) Object ID.

(2) Right ascension.

(3) Declination.

(4) Spectroscopic redshift of Ly α emission line.

(5)-(6) Total magnitudes of NB816 and z -bands.

(7) Reference (O08: Ouchi et al. 2008; H: R. Higuchi in prep.).

Note that the magnitudes are values directly obtained from the HSC catalog.